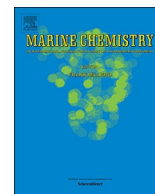




Contents lists available at ScienceDirect

## Marine Chemistry

journal homepage: [www.elsevier.com/locate/marchem](http://www.elsevier.com/locate/marchem)

# The carbon: $^{234}\text{Th}$ ratios of sinking particles in the California current ecosystem 2: Examination of a thorium sorption, desorption, and particle transport model

Michael R. Stukel<sup>a,b,\*</sup>, Thomas B. Kelly<sup>a</sup>

<sup>a</sup> Dept. of Earth, Ocean, and Atmospheric Science, Florida State University, Tallahassee, FL, United States of America

<sup>b</sup> Center for Ocean-Atmospheric Prediction Studies, Florida State University, Tallahassee, FL, United States of America

## ABSTRACT

Thorium-234 ( $^{234}\text{Th}$ ) is a powerful tracer of particle dynamics and the biological pump in the surface ocean; however, variability in carbon: thorium ratios of sinking particles adds substantial uncertainty to estimates of organic carbon export. We coupled a mechanistic thorium sorption and desorption model to a one-dimensional particle sinking model that uses realistic particle settling velocity spectra. The model generates estimates of  $^{238}\text{U}$ – $^{234}\text{Th}$  disequilibrium, particulate organic carbon concentration, and the C: $^{234}\text{Th}$  ratio of sinking particles, which are then compared to *in situ* measurements from quasi-Lagrangian studies conducted on six cruises in the California Current Ecosystem. Broad patterns observed in *in situ* measurements, including decreasing C: $^{234}\text{Th}$  ratios with depth and a strong correlation between sinking C: $^{234}\text{Th}$  and the ratio of vertically-integrated particulate organic carbon (POC) to vertically-integrated total water column  $^{234}\text{Th}$ , were accurately recovered by models assuming either a power law distribution of sinking speeds or a double log normal distribution of sinking speeds. Simulations suggested that the observed decrease in C: $^{234}\text{Th}$  with depth may be driven by preferential remineralization of carbon by particle-attached microbes. However, an alternate model structure featuring complete consumption and/or disaggregation of particles by mesozooplankton (e.g. no preferential remineralization of carbon) was also able to simulate decreasing C: $^{234}\text{Th}$  with depth (although the decrease was weaker), driven by  $^{234}\text{Th}$  adsorption onto slowly sinking particles. Model results also suggest that during bloom decays C: $^{234}\text{Th}$  ratios of sinking particles should be higher than expected (based on contemporaneous water column POC), because high settling velocities minimize carbon remineralization during sinking.

## 1. Introduction

Thorium isotopes are powerful tracers of particle cycling in the ocean. At natural seawater pH, Th exists in the Th(IV) oxidation state, which is highly particle reactive and hence rapidly scavenged from the surface ocean (Bhat et al., 1968; Coale and Bruland, 1985; Santschi et al., 2006). Multiple isotopes of Th are abundant in the ocean. While the essentially stable  $^{232}\text{Th}$  is the most abundant isotope of Th, many shorter-lived, radiogenic isotopes are produced in the ocean. Of particular utility are the isotopes  $^{234}\text{Th}$ , which is produced by decay of  $^{238}\text{U}$  and decays with a half-life of 24.1 days, and  $^{228}\text{Th}$ , which is produced by decay of  $^{228}\text{Ra}$  and has a half-life of 1.9 years.  $^{234}\text{Th}$  and  $^{228}\text{Th}$  have been used extensively for studying particle cycling in the surface and deep ocean, respectively (Buesseler et al., 1992; Luo et al., 1995; Waples et al., 2006), while longer lived isotopes of Th have been used for diverse purposes, including aggregate accumulation in deep-sea

sediments and aeolian Fe input in oligotrophic gyres (Hayes et al., 2015; Shaw et al., 1998).

Despite the clear utility of Th for investigating particle dynamics, its extensive use as an *in situ* tracer, and multiple laboratory experiments investigating its sorption and desorption kinetics in the laboratory (Reiller et al., 2008; Santschi et al., 2006; Waples et al., 2006), we cannot presently predict C:Th ratios in the ocean (Buesseler et al., 2006). This uncertainty is derived from the heterogeneity of particles in the ocean with respect to origin, size, sinking speed, fractal structure, and chemical composition. In seawater, Th(IV) binds strongly to humic acids and polysaccharides (Guo et al., 2002; Passow et al., 2006; Reiller et al., 2003), both of which are common components of marine colloidal material. A simple model with spherical particles would suggest that a surface reactive ion, such as Th(IV), should increase quadratically with particle diameter, while particle carbon mass increases approximately linearly with particle volume, leading to increasing C:Th ratios

DOI of original article: <https://doi.org/10.1016/j.marchem.2019.01.003>

Abbreviations: CCE, California Current Ecosystem; dpm, decays per minute = 1/60 Bq;  $^{\circ}\text{C}^{234}\text{Th}_{\text{tot}}$ , vertically-integrated POC / vertically-integrated total water column  $^{234}\text{Th}$ ; PLaw, Power Law Model; 2Log, Double Log Normal Model; 1Sink, Single Sinking Speed Model

\* Corresponding author at: Dept. of Earth, Ocean, and Atmospheric Science, Florida State University, Tallahassee, FL, United States of America.

E-mail address: [mstukel@fsu.edu](mailto:mstukel@fsu.edu) (M.R. Stukel).

<https://doi.org/10.1016/j.marchem.2019.03.005>

Received 17 October 2018; Received in revised form 20 January 2019; Accepted 11 March 2019

0304-4203/© 2019 Elsevier B.V. All rights reserved.

with increasing particle size. However, the multiplicity of processes that can create particles and reshape their sizes in the water column (e.g. aggregation and disaggregation, compaction into fecal pellets, *de novo* synthesis, preferential remineralization or consumption) obfuscate patterns between C:Th ratios and particle size (Buesseler et al., 2006; Burd et al., 2007).

Determining empirical and/or mechanistic models of variability in the C:<sup>234</sup>Th ratio is particularly important, because of the rapid growth of <sup>234</sup>Th as a tracer of the biological carbon pump. <sup>234</sup>Th profiles are now regularly measured on survey cruises (e.g., Owens et al., 2015; van der Loeff et al., 2011), most of which do not have sampling plans that allow deployment of sediment traps for collecting particles for determination of the C:<sup>234</sup>Th ratio, which is necessary for converting <sup>234</sup>Th flux calculations into carbon flux estimates. Instead, such studies often rely on the C:<sup>234</sup>Th ratios of size-fractionated particles collected by *in situ* pump (often at only a subset of the stations sampled for total watercolumn <sup>234</sup>Th, e.g., Puigcorb  et al., 2017) or infer the C:<sup>234</sup>Th ratio from average regional estimates determined during other studies (e.g., Ducklow et al., 2018; Estapa et al., 2015). Such an approach is problematic because C:<sup>234</sup>Th ratios can vary substantially with depth, location, and time (Buesseler et al., 2006; Hung et al., 2004; Szlosek et al., 2009). For instance, in our study region, C:<sup>234</sup>Th ratios of sinking particles in the shallow twilight zone (50–150 m), vary by nearly a factor of 10 (Stukel et al., 2019). While sediment traps may introduce their own biases during particle collection (Buesseler et al., 2007), they are more likely to sample particles representative of sinking flux than *in situ* pumps because *in situ* pumps are inherently biased towards sampling slowly sinking or suspended particles (relative to their contributions to sinking flux). Furthermore, recent studies showing the importance of < 51- m particles to sinking flux call into question the common assumption that only large particles should be considered representative of sinking material (Durkin et al., 2015; Hung et al., 2012).

Ultimately, elucidating the processes driving variability in the C:<sup>234</sup>Th of sinking particles is important for two purposes: (1) interpreting *in situ* <sup>238</sup>U–<sup>234</sup>Th measurements to estimate POC flux and (2) developing mechanistic models of <sup>234</sup>Th distributions and flux. Multiple Th sorption models have been applied to marine systems (Savoye et al., 2006, and references therein). Dunne et al. (1997) used a series of coupled phytoplankton-particle-<sup>234</sup>Th models to investigate particle cycling in the Equatorial Pacific. They found that calculations of particle sorption were dependent on model assumptions about the processes driving remineralization and that <sup>234</sup>Th was cycled between the particulate and dissolved phases multiple times prior to sinking from the euphotic zone. Burd et al. (2007) used models with phytoplankton, fecal pellets, and explicit aggregation processes to determine how C:<sup>234</sup>Th ratios would vary with size and concluded that complex biotic interactions can affect C:<sup>234</sup>Th ratios in different ways that can obfuscate attempts to estimate the C:<sup>234</sup>Th ratios of sinking particles from size-fractionated sampling approaches. Resplandy et al. (2012) coupled a relatively simple thorium sorption and desorption model to a three-dimensional physical-biogeochemical model to explore the impact of mesoscale variability on interpretations of *in situ* data. The varying complexity of these models highlight the limits of our ability to fully constrain <sup>234</sup>Th sorption dynamics in mechanistic models.

In this study, we compare the results of *in situ* POC and <sup>234</sup>Th measurements to the results of a mechanistic Th sorption and particle cycling model. *In situ* data are derived from 6 process cruises conducted with the California Current Ecosystem (CCE) Long-Term Ecological Research (LTER) Program, during which we conducted 26 quasi-Lagrangian experiments to quantify ecological and biogeochemical relationships in discrete water parcels. During each quasi-Lagrangian experiment, we quantified water column <sup>238</sup>U–<sup>234</sup>Th disequilibrium in the epipelagic and determined the C:<sup>234</sup>Th ratios of sinking particles collected by sediment trap and large particles collected by *in situ* pump. In a companion manuscript, we compared the C:<sup>234</sup>Th ratio of sinking particles to plankton community standing stock and rate measurements

that capture variability in nutrient concentrations, particulate organic matter, and phytoplankton and zooplankton ecological dynamics (Stukel et al., 2019). In the present manuscript, we couple a mechanistic <sup>234</sup>Th sorption and desorption model to a realistic, one-dimensional model of discrete particle production and sinking. We compare the results of this mechanistic model of <sup>234</sup>Th transport to field data to assess the hypothesis that relatively simple sorption and desorption equations, when coupled with realistic particle sinking speeds, can explain C:<sup>234</sup>Th variability in a dynamic coastal upwelling biome.

## 2. Methods

### 2.1. *In situ* sampling

Field measurements were made during quasi-Lagrangian experiments on 6 process cruises of the CCE LTER Program (Fig. 1): P0704 (April 2007), P0810 (October 2008), P1106 (June 2011), P1208 (August 2012), P1408 (August 2014), and P1604 (April 2016). The P0704 and P0810 cruises were focused on characterizing large-scale ecosystem variability during El Ni o-neutral conditions. Consequently, patches of water ranging from coastal, upwelling to offshore, oligotrophic conditions were chosen for study (Landry et al., 2012; Stukel et al., 2013). The P1408 and P1604 cruises were planned to quantify ecosystem rates in similar regions when climatic conditions were altered by the 2014–15 North Pacific heat anomaly and 2015–2016 El Ni os (Morrow et al., 2018; Nickels and Ohman, 2018). In contrast to these cruises, during which frontal regions were intentionally avoided when choosing water parcels to study, the P1106 and P1208 cruises investigated the biogeochemical and ecological impacts of mesoscale fronts. Quasi-Lagrangian experiments were hence conducted within, and to either side of dynamic regions with mesoscale variability (Krause et al., 2015; Stukel et al., 2017).

On each cruise, an experimental array was used to track a parcel of water for two- to five-days. The experimental array consisted of a 3 × 1-m holey sock drogue, a satellite-enabled surface drifter, and a coated cable with a series of attachment points onto which mesh bags containing incubation bottles could be attached at depths from 2 m to 110 m (Landry et al., 2009). A separate, identically drogued, sediment trap array was deployed immediately prior to the experimental array and used to collect sinking particles (see below). During each two- to five-day quasi-Lagrangian experiment (hereafter, “cycle”), the experimental array was used as a moving frame of reference for a suite of rate and standing stock measurements including: primary productivity (<sup>14</sup>CPP measured by H<sup>14</sup>CO<sub>3</sub><sup>−</sup> uptake at 6–8 depths spanning the euphotic zone), phytoplankton growth and protistan grazing rates (dilution experiments at 6–8 depths spanning the euphotic zone), phytoplankton biomass (a combination of epifluorescence microscopy and

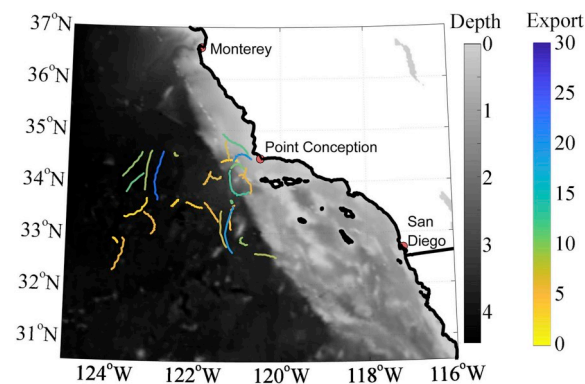


Fig. 1. Region map of the CCE study area. Gray scale is bathymetry (km). Colored lines show tracks of drifting sediment trap deployments. Color indicates measured export ( $\text{mmol C m}^{-2} \text{d}^{-1}$ ).

flow cytometry at 6–8 depths), particulate organic carbon (POC) measurements, mesozooplankton grazing rates (gut pigment measurements from day-night paired oblique bongo tows). For additional details, please see our companion manuscript (Stukel et al., 2019) and references therein.

## 2.2. Water column $^{234}\text{Th}$ measurements

$^{234}\text{Th}$  measurements were made at 8–12 depths from the surface to ~200 m using standard small volume methods (Benitez-Nelson et al., 2001; Pike et al., 2005). Typically,  $^{234}\text{Th}$  was measured on two profiles per cycle (at the beginning and end of the cycle). Additional samples were taken on each cruise from a depth of > 1000 m (and at least 1000 m from the seafloor) as an internal standard, because water at these depths is assumed to be at equilibrium with respect to  $^{238}\text{U}$ . 4-L samples were drawn from Niskin bottles into high-density polyethylene bottles, immediately acidified to a pH < 2.0 with nitric acid, and spiked with a  $^{230}\text{Th}$  yield tracer. Samples were then vigorously shaken and allowed to sit for 4–9 h. Ammonium hydroxide was then added to adjust pH to 8–9 and 100  $\mu\text{L}$  each of  $\text{KMnO}_4$  (7.5  $\text{g L}^{-1}$ ) and  $\text{MnCl}_2$  (33  $\text{g L}^{-1}$ ) were added. Samples were shaken and allowed to sit for > 8 h while  $^{234}\text{Th}$  was scavenged onto manganese oxide precipitate. Samples were then filtered through quartz (QMA) filters at high vacuum, dried in a drying oven, and mounted in RISO sampling cups. On the P0704, P0810, and P1604 cruises, samples were sent to the University of South Carolina for beta counting on a RISO multi-counter after the cruise (Stukel et al., 2011). On the P1208, P1408, and P1604 cruises, samples were counted at sea on a RISO multi-counter (Stukel et al., 2017). Background counts were performed > 6 half-lives after the cruise. For the P1408 and P1604 cruises, samples were counted an additional two to three times while they decayed to allow fitting of an exponential decay curve to each sample for improved accuracy. After background counting, samples were digested in 8 M nitric acid / 10% hydrogen peroxide solution using a sonicating water bath.  $^{229}\text{Th}$  yield tracer was then added and thorium was purified from the solution by column chromatography using Poly-Prep chromatography columns and AG1-X8 resin. Samples were eluted with hydrochloric acid, which was then evaporated off so that samples could be taken up in dilute nitric acid. Hydrofluoric acid was then added (1% final concentration) and the  $^{229:230}\text{Th}$  ratio was determined on an Element 2 inductively-coupled mass spectrometer at the Woods Hole Oceanographic Institute Analytical Facility (P0704, P0810, P1106, and P1208) or at the National High Magnetic Field Laboratory (P1408 and P1604). The  $^{229:230}\text{Th}$  ratio was then used to determine the initial filtration yield for  $^{234}\text{Th}$ .

$^{238}\text{U}$  activity was determined from salinity using the relationship in Owens et al. (2011).  $^{234}\text{Th}$  flux was determined by trapezoidally integrating  $^{238}\text{U}$ – $^{234}\text{Th}$  deficiency and using a one-dimensional, steady-state equation without upwelling (Savoie et al., 2006):  $\text{Export} = \lambda_{234} \times (^{238}\text{U} - ^{234}\text{Th})$ , where  $\lambda_{234}$  is the  $^{234}\text{Th}$  decay constant. The assumption of no upwelling may add a slight bias to our results. Although, rapid coastal upwelling is typically restricted to a narrow band closer to shore than we typically sampled, weaker wind stress curl upwelling may at times have introduced  $^{234}\text{Th}$  from below.  $\text{C}^{234}\text{Th}$  were measured on sediment trap samples (all cruises, see below) and on > 50- $\mu\text{m}$  samples collected using a McLane WTS-LV *in situ* pump and 147-mm Nitex filters (P0704, P0810, and P1106). Samples for  $\text{C}^{234}\text{Th}$  analyses were filtered through pre-combusted (450  $^\circ\text{C}$  for > 4 h) QMA filters and beta counted as above. After background counts, filters were sectioned, acidified with fuming hydrochloric acid in a desiccator, dried, placed in pre-combusted tin cups, and carbon and nitrogen were quantified by elemental analyzer at the Scripps Institution of Oceanography Analytical Facility.

## 2.3. Sediment trap deployments

VERTEX-style particle interceptor tube (PIT) sediment traps (Knauer

et al., 1979) were deployed at the beginning and recovered at the end of each experimental cycle, for a typical deployment duration ranging from 2.25 to 4.25 days (one deployment was for only 1.25 days; two had longer durations of 5.2 and 5.6 days). PIT arrays consisted of one to three PVC crosspieces holding eight to twelve tubes. Crosspieces were set at 100 m on each cruise. On all cruises except P0704 an additional crosspiece was placed at a depth slightly deeper than the euphotic zone (if the euphotic zone, as determined at sea from fluorescence profiles was shallower than 80 m). On the P1408 and P1604 cruises, an additional crosspiece was placed at 150 m. On the P1604 cruise, the array line was bitten by a shark and had to be re-spliced. Consequently sampling depths were 3 m shallower than intended. Tubes were constructed from 610-mm long, 70-mm inner diameter acrylic. A 76-mm long baffle constructed from 13 beveled tubes (12.7-mm inner diameter) was attached to the top of each tube to minimize mixing during deployment and recovery and to create minimize hydrodynamic biases in particle collection efficiency.

Tubes were filled with a saltwater brine consisting of 0.1- $\mu\text{m}$  filtered surface seawater, amended with 50  $\text{g L}^{-1}$  NaCl. Buffered formaldehyde was added to a final concentration of 0.4%. Immediately after recovery (within 30 min) the interface separating trap brine from overlying seawater was determined and overlying seawater was drawn down to ~3-cm above the interface by gentle suction. Samples were then gravity filtered through a 202- $\mu\text{m}$  nitex filter and these filters were examined used a stereomicroscope to allow removal of swimming metazoan zooplankton. After removal of “swimmers” from the samples, the non-swimmer portion of the samples were typically rinsed back into the < 202- $\mu\text{m}$  sample (although on the P1208, P1408, and P1604 cruises,  $\text{C}^{234}\text{Th}$  was analyzed separately on small and large size fractions). Samples were then split using a Folsom splitter for a suite of analyses. Typically, full tubes were filtered through pre-combusted QMA filters for  $\text{C}^{234}\text{Th}$  analysis (in triplicate, analyzed as above) and 1/4 to 1/2 tube splits were filtered through pre-combusted glass fiber (GF/F) filters for organic carbon and nitrogen analyses (analyzed at the Scripps Institution of Oceanography Analytical Facility using either an elemental analyzer or an isotope ratio mass spectrometer).

## 3. Model description

To mechanistically model  $^{234}\text{Th}$  distributions and  $\text{C}^{234}\text{Th}$  ratios during our cycles, we combined a discrete particle creation and sinking model (Stukel et al., 2018b) with an Eulerian  $^{234}\text{Th}$  sorption and desorption model (Resplandy et al., 2012). The particle model (see *Discrete particle model* section below) created particles at rates determined by *in situ* primary productivity measurements and assigned them with sinking speeds determined from realistic sinking speed distributions parameterized separately for each cycle. The particles then sank and were diffused in a one-dimensional model of the upper 200 m of the water column. At each time-step, the total POC contained in the particles in each model layer (1 m vertical resolution) was summed to map POC into an Eulerian framework (see *Eulerian  $^{234}\text{Th}$  sorption and desorption model*). Upwelling was not included in the model. We assumed that vertical eddy diffusivities ( $K_z$ , for particles and dissolved  $^{234}\text{Th}$ ) were equal to  $10^{-4} \text{ m}^2 \text{ s}^{-1}$  in the mixed layer (defined from field data as the depth at which density increased by 0.125  $\text{kg m}^{-3}$  relative to the surface) and decreased gradually to  $10^{-5} \text{ m}^2 \text{ s}^{-1}$  at a depth of twice the mixed layer. The model was spun up (starting with  $^{234}\text{Th}$  at equilibrium with  $^{238}\text{U}$  and no POC) for 90 days and results were then analyzed for 4 consecutive days. Model time step was 1 min for Eulerian diffusion and 1 h for all other processes.

### 3.1. Discrete particle model

We used the discrete particle creation, remineralization, and sinking modeling framework of Stukel et al. (2018b). Unlike most biogeochemical models, which assume fixed *a priori* sinking speeds for sinking

particles, this approach assumes that actual particles have a range of sinking speeds that can be modeled using some probability density function. If the shape of this function is known (or assumed) and dependent on a limited number of parameters (including remineralization rate), *in situ* data (e.g. primary productivity, POC concentrations, and carbon export) can be used to constrain the PDF. The resultant function will thus create, remineralize, and sink particles at rates that are consistent with the *in situ* measurements. The resultant model is thus not mechanistic in terms of predicting properties that impact the sinking speed of particles but it does predict realistic particle sinking dynamics that can be used to mechanistically investigate the interactions between sinking particles and other properties of the system (e.g.  $^{234}\text{Th}$ ).

Stukel et al. (2018b) suggested two plausible functions to describe particle production as a function of sinking speed (PP(S)). The first posited that there were two classes of sinking particles (phytoplankton and fecal pellets) and that the sinking speeds of each of these particles could be described as a log-normal distribution:

$$PP_{2Log}(S) = \tau \frac{1 - \Phi}{\sigma_1 \sqrt{2\pi} S} \exp\left(-\frac{(\ln(S) - \mu_1)^2}{2\sigma_1^2}\right) + \tau \frac{\Phi}{\sigma_2 \sqrt{2\pi} S} \exp\left(-\frac{(\ln(S) - \mu_2)^2}{2\sigma_2^2}\right) \quad (1)$$

where  $\tau$  is the total particle production rate,  $\Phi$  is the ratio of fecal pellet production to total, and  $\mu_1$  and  $\mu_2$  are parameters related to the median sinking rate of phytoplankton and fecal pellets, respectively. Rather than set the sinking rate for either phytoplankton or fecal pellets, Stukel et al. (2018b) assumed that the median sinking speed for fecal pellets was 100 times greater than the one for phytoplankton, thus, since the median of a log-normal distribution is equal to  $\exp(\mu)$ ,  $\mu_2 = \ln(100 \times \exp(\mu_1))$ . This assumption was based on studies that have shown sinking speeds for individual phytoplankters to be on the order of  $1 \text{ m d}^{-1}$  (e.g. Smayda and Bienfang, 1983), while mesozooplankton fecal pellet sinking velocities are on the order of  $100 \text{ m d}^{-1}$  (Turner, 2002). Stukel et al. (2018b) also assumed that the coefficients of variation for sinking speeds of the two particle types were both equal to 1 ( $\sigma_1 = \sigma_2 = 1$ ).

The second distribution of sinking speeds was inspired by the power law relationships between aggregate sinking speed and aggregate size and between aggregate abundance and aggregate size:

$$PP_{PLaw}(S) = \alpha \times S^\beta \quad (2)$$

where  $\alpha$  and  $\beta$  are parameters related to the specific ecological and chemical conditions experienced *in situ* and hence must be determined empirically. Although, Stukel et al. (2018b) referred to these models as the phytoplankton-fecal pellet and aggregate models, respectively, we refer to them here as the Double Log Normal (2Log) and Power Law (PLaw) models to make it clear that these models do not include mechanistic representations of fecal pellet production or aggregate formation.

In addition to the 2Log and PLaw models, we also introduce a model that mimics the sinking approach used in most three-dimensional biogeochemical models. In this model (which we refer to as the Single Sinking Speed, or 1Sink model) particles are either not sinking or sink at a speed of  $\omega$ . Sinking speed distributions can thus be written as:

$$PP_{1Sink}(0) = \Pi \times (1 - \epsilon) \quad \text{if } S = 0 \quad (3a)$$

$$PP_{1Sink}(\omega) = \Pi \times \epsilon \quad \text{if } S = \omega \quad (3b)$$

where  $\Pi$  is the total production rates of particles and  $\epsilon$  is the fraction of particles that are sinking.  $\omega$  was set to  $100 \text{ m d}^{-1}$  based on *in situ* results from McDonnell and Buesseler (2010). We note that while this model was created to mimic the behavior of typical biogeochemical models, it is still distinct in that it is a discrete particle model, not a concentration-based model.

Our goal in using these alternate sinking speed distributions is not to

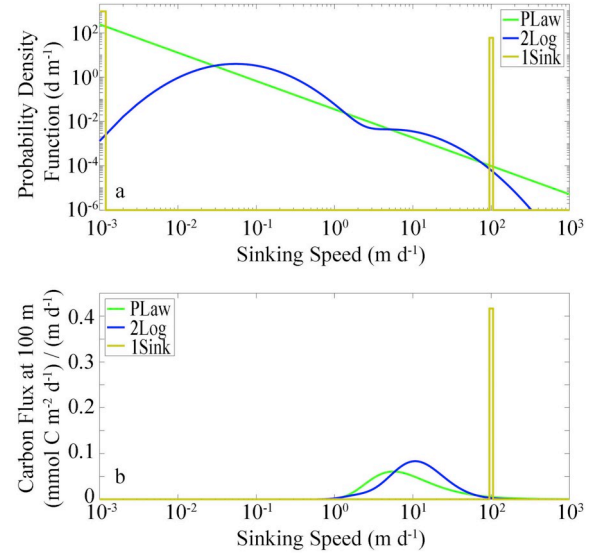


**Fig. 2.** Particle sinking speed spectra. (a) Particle production as a function of sinking speed for the Power Law (green), Double Log-Normal (blue), and Single Sinking Speed (yellow) models. (b) Export flux at 100 m as a function of particle sinking speed. Both plots are for Cycle 0704-2. Note that plots for the 1Sink model are illustrative (not true probability density functions) because particle sinking speeds are discrete (either 0 m or 100 m) for the 1Sink model. (For interpretation of the references to colour in this figure legend, the reader is referred to the web version of this article.)

suggest that any of them is an accurate reflection of true variability in particle sinking speeds. *In situ* sinking speeds are set by a complex interplay of processes including particle production by diverse phytoplankton taxa, aggregation of these particles into sinking marine snow, packaging of particles into dense fecal pellets, and mineral ballasting effects mediated by diverse phyto- and zooplankton groups (Armstrong et al., 2009; Jackson and Burd, 2015; Steinberg and Landry, 2017; Turner, 2015). Rather, our goal was to produce plausible alternate possibilities (Fig. 2) that could be used to test model sensitivity.

To define the parameters  $\mu$ ,  $\Phi$ , and  $\tau$  in Eq. 1,  $\alpha$  and  $\beta$  in Eq. 2, or  $\Pi$  and  $\epsilon$  in Eq. 3, we used data from the Lagrangian experiments detailed in Section 2. Specifically, organic carbon export (determined by sediment trap), particle production rates (determined from  $^{14}\text{CPP}$ ), and POC standing stock (vertically-integrated over the euphotic zone) can be used to solve for a remineralization constant for particles ( $\gamma$ , units of  $\text{d}^{-1}$ ) and two parameters from Eqs. 1, 2, or 3. If particle production is assumed to be concentrated at a depth of  $d_{\text{prod}}$  (which was determined experimentally as the mean depth of  $^{14}\text{CPP}$ ), we can relate the flux of particles as a function of depth and sinking speed to PP(S) through the following equation:

$$\text{Flux}(z, S) = PP(S) \times e^{-\gamma(z-d_{\text{prod}})/S} \quad (4)$$

We can then relate parameters measured *in situ* to PP(S) and Flux( $z, S$ ) using the following equations:

$$^{14}\text{CPP} = \int_{S=S_{\text{min}}}^{S=S_{\text{max}}} PP(S) dS \quad (5)$$

$$\text{Export}_{z=100} = \int_{S=S_{\text{min}}}^{S=S_{\text{max}}} \text{Flux}(100, S) dS \quad (6)$$

$$\text{POC}_{\text{total}} = \int_{z=d_{\text{prod}}}^{z=d_{\text{POC}}} \int_{S=S_{\text{min}}}^{S=S_{\text{max}}} C(z, S) dS dz \quad (7)$$

where  $d_{\text{POC}}$  is the deepest depth at which POC measurements are made (if shallower than 100 m).  $C(z, S)$  is the POC concentration in particles

of a sinking speed  $S$  at a depth of  $z$  and can be calculated from the equation:

$$C(z, S) = \frac{\text{Flux}(z, S)}{S} \quad (8)$$

Since  $\Phi$  in Eq. 1 could be determined directly by assuming an egestion efficiency of 30% (Conover, 1966) and comparing the ratio of mesozooplankton grazing to  $^{14}\text{CPP}$ , the remaining parameters in Eqs. 1–3 (and  $\gamma$ ) could be solved using Eqs. 5–7. We solved these equations using a grid search in Matlab for each individual Lagrangian experiment (Fig. 2, Supp. Table 1). For additional details on the derivations of Eq. 1–8, see Stukel et al. (2018b).

Eqs. 1–3 were then used to generate particle sinking speeds for discrete particles that were initialized in a 1-D model at depths determined by the  $^{14}\text{CPP}$  vertical profiles for a specific Lagrangian experiment (Supp. Fig. 1.1). Typically, 10,000 super particles (*i.e.*, each represents multiple particles with similar properties) were created per day and each was initialized with an organic carbon content that was proportional to measured vertically-integrated  $^{14}\text{CPP}$  (*e.g.* for typical  $^{14}\text{CPP}$  values of  $100 \text{ mmol C m}^{-2} \text{ d}^{-1}$ , each particle would represent  $0.01 \text{ mmol C m}^{-3}$ ). Each particle was set to sink at its pre-determined sinking speed (different for each particle), was remineralized based on the estimated  $\gamma$  (constant for all particles from a specific Lagrangian cycle), and was diffused based on the vertical eddy diffusivity at its current depth (see above).

**Eulerian  $^{234}\text{Th}$  sorption and desorption model** – We used the thorium sorption and desorption model of Resplandy et al. (2012), with modifications to run in concert with our discrete particle model. The model uses second order rate kinetics for  $^{234}\text{Th}$  adsorption onto particles:

$$\text{Adsorption} = k_1 \times \text{POC}(z) \times \text{Th}_d(z) \quad (9)$$

where  $\text{POC}(z)$  is the summed POC concentration of all discrete particles within a layer, and  $\text{Th}_d(z)$  is the activity of dissolved  $^{234}\text{Th}$  in the layer. Some prior thorium sorption models have used first-order kinetics equations for thorium sorption ( $\text{Absorption} = k_1' \cdot \text{Th}_d$ , where  $k_1'$  is equivalent to our  $k_1/\text{POC}$ ), thus implicitly assuming that  $^{234}\text{Th}$  adsorption is actually independent of POC concentration (Black et al., 2018; Dunne et al., 1997; Lerner et al., 2016). However, detailed analysis of the results of first-order kinetics models have repeatedly detected a particle-concentration effect showing that  $k_1'$  is positively correlated with POC as would be expected if thorium sorption follows second-order kinetics (Black et al., 2018; Lerner et al., 2016). Hence we believe that the second-order model of Resplandy et al. (2012) is more appropriate, especially in regions (such as the CCE) with high variability in POC concentration.

$^{234}\text{Th}_d$  (and  $^{238}\text{U}$ ) were modeled in a one-dimensional Eulerian framework with 200 one-meter thick layers extending from the surface to 200-m depth. At each model time-step, Eq. 9 was used to adsorb  $^{234}\text{Th}$  from the dissolved pool to the particulate pool. This  $^{234}\text{Th}$  was distributed to all particles within a layer in proportion to their POC content.  $^{234}\text{Th}$  desorption is calculated with a first-order rate law:

$$\text{Desorption} = k_{-1} \times \text{Th}_p(z) \quad (10)$$

where  $\text{Th}_p$  is the activity of  $^{234}\text{Th}$  on all particles within the layer.  $^{234}\text{Th}$  desorbing from particles is passed to the dissolved  $^{234}\text{Th}$  pool for the layer in which the particle resides. For  $k_{-1}$  (the desorption constant), we used a value of  $3 \text{ yr}^{-1}$  (as used in Resplandy et al., 2012). For  $k_1$  (the adsorption constant), we used a value of  $0.013 \text{ m}^3 \text{ mmol C}^{-1} \text{ d}^{-1}$  (the median value for the CCE, calculated in Stukel et al., 2019).  $\text{Th}_d$  is produced by radioactive decay from  $^{238}\text{U}$  ( $U(z)$ ; which was held at constant values as determined from *in situ* salinity profiles and a salinity- $^{238}\text{U}$  relationship).  $\text{Th}_p$  and  $\text{Th}_d$  are also lost to radioactive decay.

When new particles were created in a layer, we redistributed  $\text{Th}_p$  from existing particles to the new particles in proportion to the ratio of newly created POC to total POC. This essentially mimics a process in which new particles are created from old particles thus temporarily

decreasing the C: $^{234}\text{Th}$  ratio of bulk particulate material. We also note that we do not include particle remineralization as a loss term from  $\text{Th}_p$ . This essentially parameterizes a situation in which microbes preferentially remineralize carbon, while  $^{234}\text{Th}$  is only lost from the particles due to desorption or radioactive decay. For the sensitivity of our model to this *a priori* assumption, see Discussion.

### 3.2. Model governing equations

As explained in the previous sections, our model joins a discrete particle model that tracks POC and particulate  $^{234}\text{Th}$  with an Eulerian model of dissolved  $^{234}\text{Th}$ . At each time-step (1 h) particles were created and assigned an initial depth determined from vertical profiles of *in situ* primary production, an initial carbon content equal to  $^{14}\text{CPP}/N \times dt$  (where  $N$  = the number of particles created during the time step), and a sinking speed drawn from Eqs. 1, 2, or 3 (depending on which sinking speed model was being used). Particulate  $^{234}\text{Th}$  is then re-distributed from existing particles within the layer to the new particles such that the new particles have a C: $^{234}\text{Th}$  ratio equal to the average C: $^{234}\text{Th}$  ratio in the layer. This mimics what we might expect if new particles are created from existing particles through photosynthesis.

The rate of change of dissolved  $^{234}\text{Th}$  ( $\text{Th}_d$ ) was governed by the differential equation:

$$\begin{aligned} \frac{\partial \text{Th}_d(z, t)}{\partial t} = & \lambda(U(z) - \text{Th}_d(z, t)) - k_1 \times \text{Th}_d(z, t) \times \sum_{i=z_1}^{i=z_n} \text{PC}_i \\ & + k_{-1} \times \sum_{i=z_1}^{i=z_n} \text{Th}_{p,i} + \frac{\partial}{\partial z} \left( K_z \frac{\partial \text{Th}_d(z, t)}{\partial z} \right) \end{aligned} \quad (11)$$

$\text{PC}_i$  is the organic carbon content of particle  $i$ ,  $\text{Th}_{p,i}$  is the  $^{234}\text{Th}$  activity of particle  $i$ , the sum from  $z_1$  to  $z_n$  represents a summation over all the particles within layer  $z$ , and  $V$  is the volume of layer  $z$ . Note that since each model particle actually represents multiple particles with similar properties in the water column, we use units of  $\text{mmol C m}^{-3}$  and  $\text{dpm m}^{-3}$  for  $\text{PC}_i$  and  $\text{Th}_{p,i}$ , respectively. The rate of change of  $^{234}\text{Th}$  and organic carbon on each individual particle is governed by the equations:

$$\frac{\partial \text{Th}_{p,i}(t)}{\partial t} = k_1 \times \text{Th}_d(z, t) \times \text{PC}_i + k_{-1} \times \text{Th}_{p,i} - \lambda \times \text{Th}_{p,i} \quad (12)$$

$$\frac{\partial \text{PC}_i(t)}{\partial t} = -\gamma \times \text{PC}_i \quad (13)$$

The depth of each particle is modified by the following differential equation:

$$\frac{\partial Z_i(t)}{\partial t} = -S_i + R_n \times \sqrt{2K_z/\partial t} \quad (14)$$

where  $Z_i$  is the depth of particle  $i$ ,  $S_i$  is the sinking speed of particle  $i$ , and  $R_n$  is a random number drawn from a unit normal distribution to simulate diffusion. Eqs. 12–14 can be combined with particle production (as described above) to write:

$$\begin{aligned} \frac{\partial \text{Th}_p(z, t)}{\partial t} = & k_1 \text{Th}_d(z, t) \text{POC}(z) - (\lambda + k_{-1}) \text{Th}_p(z, t) \\ & - \int_{S=0}^{S=1000} S \frac{\partial \text{Th}_p(S, z, t)}{\partial z} dS + \frac{\partial}{\partial z} \left( K_z \frac{\partial \text{Th}_p(z, t)}{\partial z} \right) \end{aligned} \quad (15)$$

$$\begin{aligned} \frac{\partial \text{POC}(z, t)}{\partial t} = & \text{PP}(z) - \gamma \text{POC}(z, t) - \int_{S=0}^{S=1000} S \frac{\partial \text{POC}(S, z, t)}{\partial z} dS \\ & + \frac{\partial}{\partial z} \left( K_z \frac{\partial \text{POC}(z, t)}{\partial z} \right) \end{aligned} \quad (16)$$

## 4. Results

### 4.1. *In situ* C:<sup>234</sup>Th variability

*In situ* variability in biomass and productivity was high across the water parcels studied during our Lagrangian cycles. Mean surface primary productivity varied by more than two orders of magnitude from 0.17 to 17  $\mu\text{mol C L}^{-1}$ . Vertically-integrated primary productivity showed slightly lower variance, ranging from 9.9 to 191  $\text{mmol C m}^{-2} \text{d}^{-1}$ , because lower biomass water parcels had deeper euphotic zones. Surface chlorophyll (Chl) ranged from 0.07 to 4.2  $\mu\text{g Chl a L}^{-1}$ . These differences in productivity and biomass drove accompanying changes in carbon export (as determined by sediment traps), which ranged from 2.6 to 25  $\text{mmol C m}^{-2} \text{d}^{-1}$  at the 100-m depth horizon and was positively correlated ( $p < 0.01$ ) with primary productivity, surface Chl, and particulate organic carbon concentrations.

<sup>234</sup>Th flux into sediment traps agreed well with estimates based on <sup>238</sup>U–<sup>234</sup>Th deficiency and a simple one-dimensional steady-state model (Fig. 3a). The mean <sup>234</sup>Th export flux measured by sediment trap was 1.01 times greater than the mean flux computed from <sup>238</sup>U–<sup>234</sup>Th deficiency and a one-dimensional steady-state equation. The median ratio of sediment trap flux to steady-state flux was 0.89. The correlation between sediment trap and steady-state estimated flux was 0.51 (Spearman's rank correlation,  $p < 10^{-3}$ ). This correlation was decreased substantially, however, by cruises P1106 and P1208, which focused on quantifying variability across mesoscale features. The residence time of water parcels in these features (days to a week), was much faster than the length of time required for <sup>234</sup>Th concentrations to reach steady state but was similar to the deployment duration of our sediment traps. The correlation between sediment trap <sup>234</sup>Th flux and steady-state estimated flux increased to 0.61 when these two cruises were excluded from the dataset. Notably, even for these two cruises, the difference between mean cruise <sup>234</sup>Th flux measured in sediment traps and estimated from <sup>238</sup>U–<sup>234</sup>Th deficiency was only 1% for P1106 and 14% for P1208. Taken together, this evidence suggests that our sediment traps exhibited no substantial over- or under-collection bias, and we conclude that they were accurately measuring the C:<sup>234</sup>Th ratio of sinking particles. We note, however, that we cannot exclude the possibility that they were under-collecting classes of particles with low <sup>234</sup>Th activity (e.g., mesozooplankton carcasses; Stukel et al., 2019).

Variability in the C:<sup>234</sup>Th ratio of sinking material in the upper twilight zone (47 to 150 m) was substantial. Sediment trap C:<sup>234</sup>Th ratios varied from 2.3 to 20.5  $\mu\text{mol C dpm}^{-1}$ . C:<sup>234</sup>Th ratios were typically higher for sinking material collected by sediment trap than for large suspended material (> 50- $\mu\text{m}$ ) collected by *in situ* pump, often by a factor of  $\sim 2$  (Fig. 3b). Large sinking material (> 200- $\mu\text{m}$ ) also typically had higher C:<sup>234</sup>Th ratios than small (< 200- $\mu\text{m}$ ) sinking material (Fig. 4c). C:<sup>234</sup>Th ratios also decreased with increasing depth. This depth dependence was best fit by a power law regression,

$$C: {}^{234}\text{Th}_{ST} = 1925 \times \text{depth}^{-1.29} \quad (17)$$

where depth is in meters and C:<sup>234</sup>Th of sediment trap material is in  $\mu\text{mol dpm}^{-1}$ . Stukel et al. (2019) used multiple linear regression to identify two relationships that strongly predicted C:<sup>234</sup>Th<sub>ST</sub> from water column properties:

$$\log_{10}(C: {}^{234}\text{Th}_{ST}) = 0.45 - 0.003 \times \text{depth} + 0.37 \times \log_{10}(\text{VertIntChl}) \quad (18)$$

where VertIntChl is vertically-integrated chlorophyll *a* ( $\text{mg Chl m}^{-2}$ ) and:

$$\log_{10}(C: {}^{234}\text{Th}_{ST}) = 0.53 + \log_{10}({}^{\text{v}}C: {}^{234}\text{Th}_{\text{tot}}) \quad (19)$$

where <sup>v</sup>C:<sup>234</sup>Th<sub>tot</sub> is the ratio of vertically-integrated POC to vertically-integrated total water column <sup>234</sup>Th above the sediment trap depth. The former equation suggests that C:<sup>234</sup>Th ratios are positively correlated with total autotroph biomass (Fig. 4a), while the second equation suggests a quantitative relationship between the C:<sup>234</sup>Th ratio of sinking material and the total POC and water column <sup>234</sup>Th inventory in the upper water column (Fig. 4b). For further details of the relationship between C:<sup>234</sup>Th ratios and biological and chemical properties in the water column, see our companion manuscript (Stukel et al., 2019).

### 4.2. Parameterization of the Lagrangian particle sinking model

We used *in situ* measurements of vertically-integrated POC and <sup>14</sup>C primary productivity and organic carbon export at the 100-m depth horizon to constrain particle production rates, sinking speed distributions, and remineralization rates for the PLaw, 2Log, and 1Sink models (the ratio of mesozooplankton grazing to phytoplankton production was also used to constrain  $\Phi$  for the 2Log model). For the PLaw model,

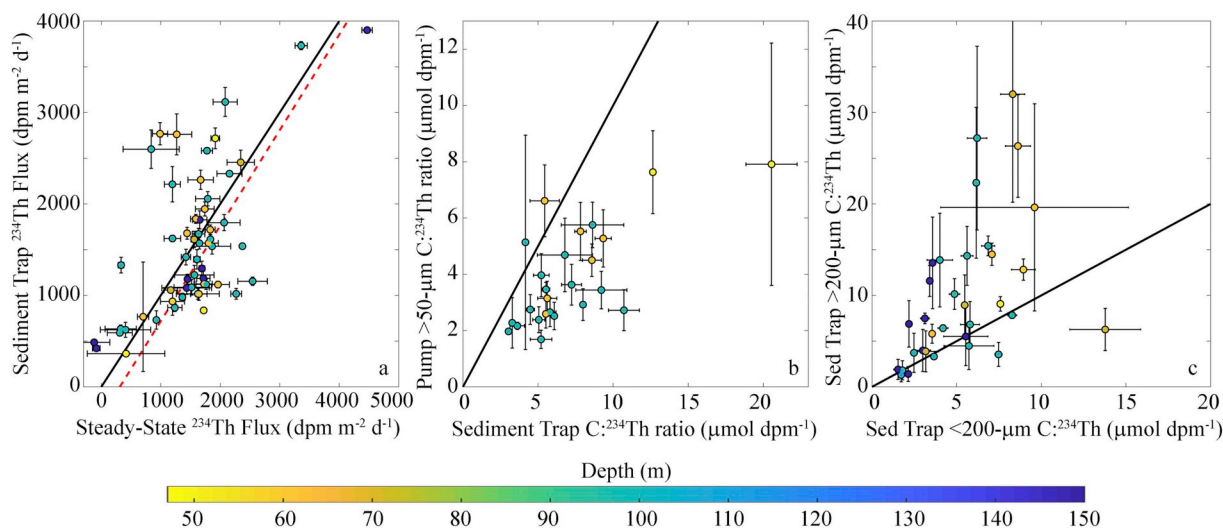


**Fig. 3.** Sediment trap and <sup>234</sup>Th measurements. (a) <sup>234</sup>Th flux determined from <sup>238</sup>U–<sup>234</sup>Th deficiency (x-axis) and measured simultaneously in sediment traps (y-axis). Red line is a type II linear regression ( $y = 1.04 \times x - 325$ ). (b) C:<sup>234</sup>Th ratio of particles collected by sediment trap (x-axis) and of > 50- $\mu\text{m}$  particles collected by *in situ* pump (y-axis). (c) C:<sup>234</sup>Th ratios of < 200- $\mu\text{m}$  (x-axis) and > 200- $\mu\text{m}$  particles collected by sediment traps. Black line is the 1:1 line in all plots, symbol colors indicate depth, and error bars show 1 standard error. (For interpretation of the references to colour in this figure legend, the reader is referred to the web version of this article.)

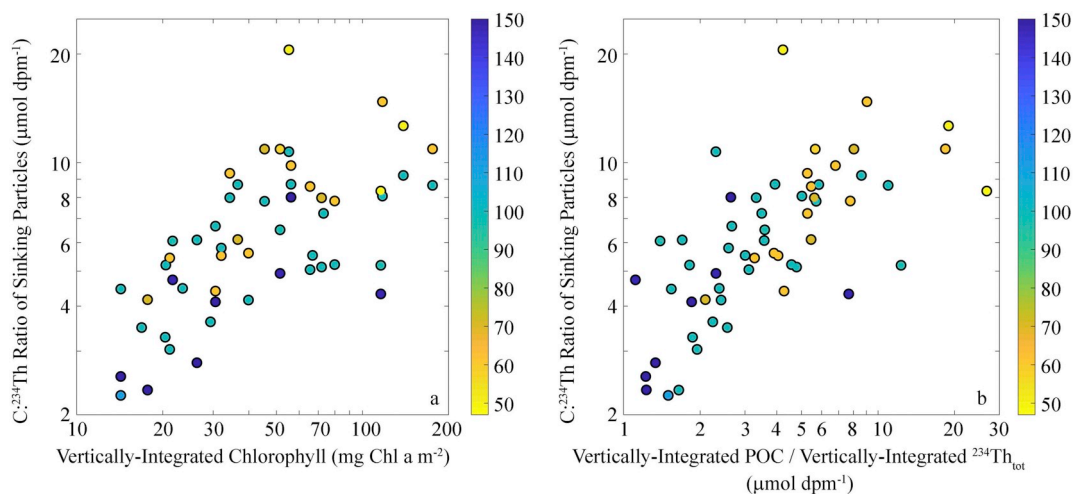


Fig. 4. Relation of C: $^{234}\text{Th}$  ratios of sinking particles to (a) vertically-integrated Chl and to (b) the ratio of vertically-integrated POC to vertically-integrated total water column  $^{234}\text{Th}$ . Note log scales in both plots. Symbol colors indicate sampling depth.

$\beta$ , which parameterizes the slope of the particle sinking speed spectrum, varied from  $-1.27$  to  $-0.87$  and  $\alpha$ , which reflects the magnitude of particle creation at a sinking speed of  $1 \text{ m d}^{-1}$ , varied from  $0.7$  to  $9.8$ . Meanwhile, the remineralization rate constant ( $\gamma$ ), varied from  $0.01$  to  $0.33 \text{ d}^{-1}$ . For the 2Log model,  $\mu_1$  (the base 10 logarithm of the median sinking speed of slowly-sinking particles) varied from  $-2.4$  to  $1.0$ , which equates to a median sinking speed of  $0.004$  to  $10 \text{ m d}^{-1}$  and  $\gamma$  varied from  $0.01$  to  $0.33 \text{ d}^{-1}$ .  $\Phi$ , which represented the ratio of production of rapidly-sinking particles (fecal pellets) to slowly-sinking particles (*i.e.*, phytoplankton) ranged from  $0.01$  to  $0.49$ .  $\tau$ , which represented the total particle production rate, was set to the measured  $^{14}\text{CPP}$ , which varied from  $9.9$  to  $191 \text{ mmol C m}^{-2} \text{ d}^{-1}$ . For the 1Sink model,  $\varepsilon$  (the ratio of sinking to non-sinking particles) ranged from  $0.06$  to  $0.51$  and  $\gamma$  varied from  $0.02$  to  $0.32 \text{ d}^{-1}$ . Meanwhile,  $\Pi$ , the total particle production rate, was set to the measured  $^{14}\text{CPP}$  values as for the 2Log model. For the full model parameterizations, see Supp. Table 1.

#### 4.3. $^{234}\text{Th}$ model-data comparison

Model-data comparisons of vertical profiles of POC and total water column  $^{234}\text{Th}$  are shown in Figs. 5 and 6, respectively (and Supp. Fig. 2). The discrete particle models broadly captured major variability in the *in situ* data. The models accurately depicted near surface maxima in POC for most of the cycles and gradual decreases with depth. They also typically correctly predicted the magnitude of POC in the mixed layer to within the variability found in the *in situ* data and correctly predicted subsurface maxima for some Lagrangian cycles (*e.g.* P1408-1). The 2Log model generally predicted slightly deeper distributions of POC than the PLaw or 1Sink models, although whether this was a more

accurate representation of *in situ* POC profiles varied between cycles. The model also developed reasonable vertical profiles of  $^{234}\text{Th}$ .  $^{234}\text{Th}$  was consistently drawn down in the mixed layer and often exhibited a zone of  $^{234}\text{Th}$  excess in the deep euphotic zone, before returning to near equilibrium with  $^{238}\text{U}$  at deeper depths. When there were discrepancies between the model and the data, they typically involved too much model  $^{234}\text{Th}$  deficiency at the surface and/or a larger than measured  $^{234}\text{Th}$  excess in midwater depths. The greatest single discrepancy between the model and the data was for cycle P1604-4. On this cycle, all three models accurately predicted incredibly low  $^{234}\text{Th}$  inventories in surface waters, but substantially overestimated  $^{234}\text{Th}$  at all depths beneath the mixed layer. This model-data discrepancy may have arisen from interactions with non-biological particles, because this cycle was one of only two cycles that was conducted on the shelf, with an initial bottom depth of only  $\sim 500 \text{ m}$ , and water column properties indicative of recent upwelling.

All three models also did a reasonable job of estimating carbon export (Fig. 7a – c). This was not surprising, since export measurements at  $100 \text{ m}$  were used to parameterize the models. However, the models were also reasonably accurate at estimating carbon export for the shallower or deeper sediment trap depths. The PLaw model and, especially, the 2Log model did an accurate job of recovering these measured values. The 1Sink model was slightly less accurate, because it underestimated flux attenuation with depth (*i.e.*, it usually predicted similar carbon export values at the base of the euphotic zone,  $100 \text{ m}$ , and  $150 \text{ m}$ ).

The PLaw and 2Log models also did a reasonable job of estimating C: $^{234}\text{Th}$  ratios of sinking material. For the PLaw model, the mean and standard deviation of the model results (across all cycles and depths at

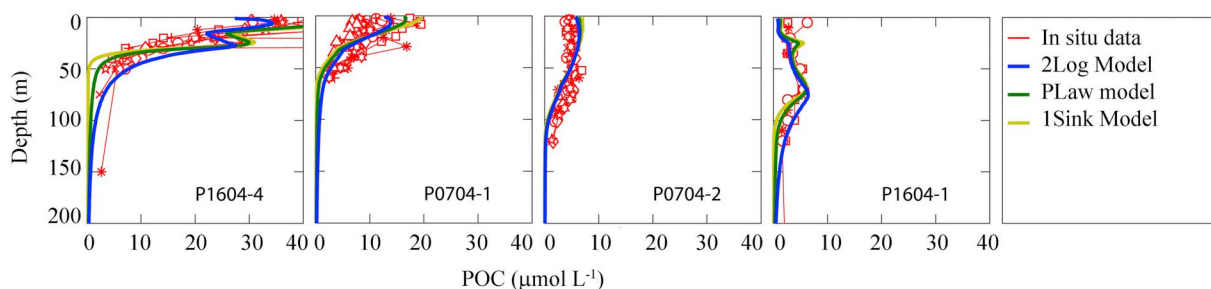
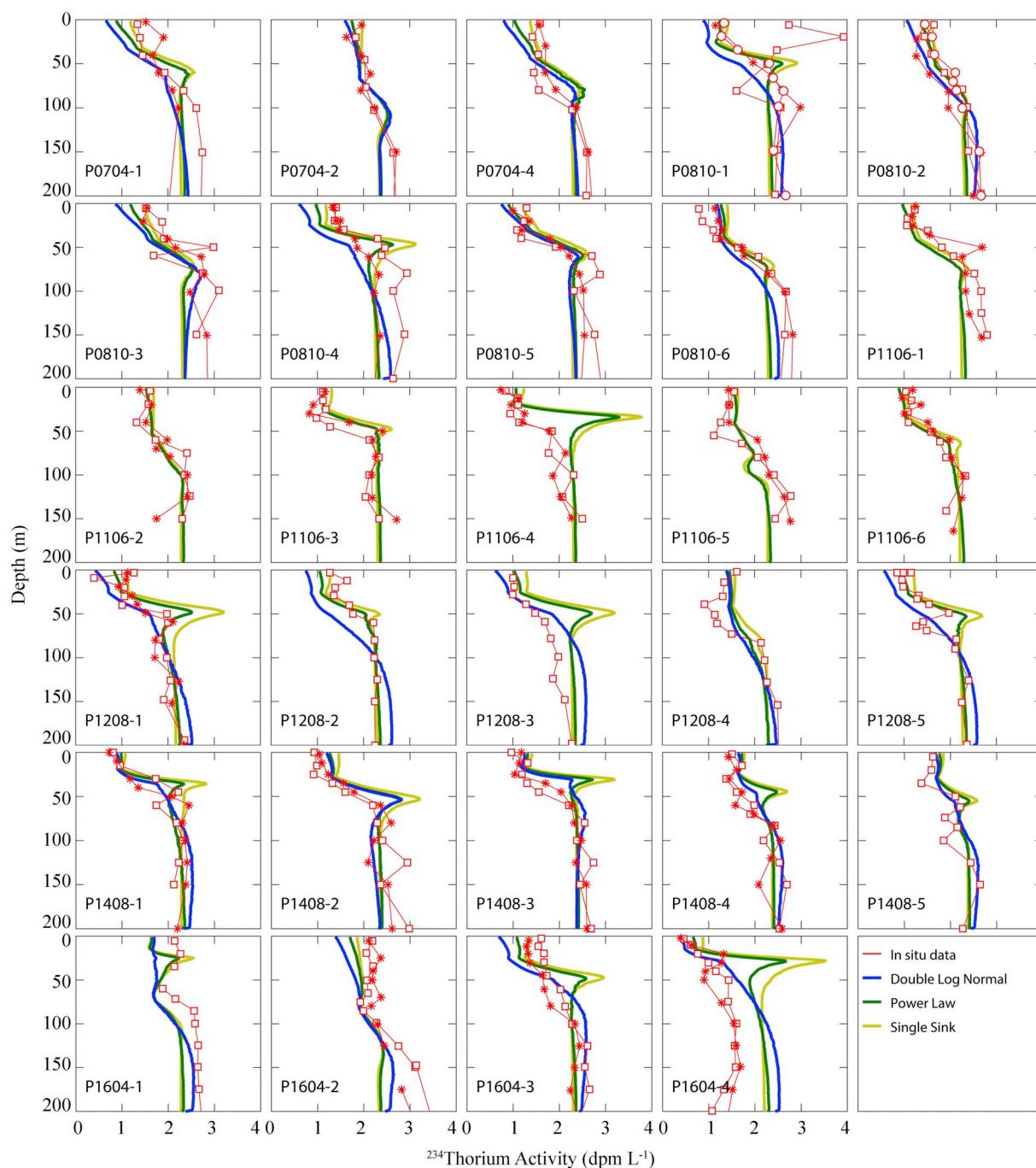


Fig. 5. Representative vertical profiles of POC as measured in the field (red traces, with each symbol representing a different cast on a Lagrangian cycle) or determined by the Power Law model (green), Double Log Normal model (blue), or Single Sinking Speed model (yellow). Plots are organized from high biomass (left) to low biomass (right). For plots from all cycles, see Supp. Fig. 1. (For interpretation of the references to colour in this figure legend, the reader is referred to the web version of this article.)



**Fig. 6.** Vertical profiles of total water column  $^{234}\text{Th}$  as measured in the field (red traces, with each symbol representing a different cast on a Lagrangian cycle) or determined by the Power Law model (green), Double Log Normal model (blue), or Single Sinking Speed model (yellow). (For interpretation of the references to colour in this figure legend, the reader is referred to the web version of this article.)

which measurements were taken) were  $6.8 \pm 3.8$ , compared to an *in situ* mean and standard deviation of  $6.8 \pm 3.3$ . For the 2Log model, the mean and standard deviation were  $5.9 \pm 3.8$ , compared to *in situ* values of  $6.6 \pm 3.4$  (note that *in situ* data were slightly different for the two models because the 2Log model could not be run for the P1106 cruise for which mesozooplankton grazing rate measurements were not available). Thus both models did a reasonable job of recovering the mean  $C:^{234}\text{Th}$  ratios and the range of variability experienced *in situ*. The model  $C:^{234}\text{Th}$  values were also within 50% of the *in situ* data for 78% of the samples with the PLaw model and 80% of the samples with the 2Log model (Fig. 7d,e). For the 1Sink model, the model  $C:^{234}\text{Th}$  values were only within 50% of the measured value 60% and were often over-

underestimated by substantial amounts (Fig. 7f).

Model vertically-integrated POC in the upper euphotic zone (upper 25 m) was also compared to the data. All models showed reasonable agreement with the *in situ* measurements (Fig. 8a). The PLaw and 2Log models slightly underestimated POC in the upper euphotic zone for most cycles, while the 1Sink model slightly overestimated it. All three models showed a strong correlation with measured POC.

Comparison of vertically-integrated  $^{234}\text{Th}$  (upper 50 m) between the models and data showed much poorer results. Vertically-integrated  $^{234}\text{Th}$  estimates (to 100 m depth) predicted by the model were generally of the same order of magnitude as the measurements. The measured vertically-integrated  $^{238}\text{U}-^{234}\text{Th}$  deficiency was  $-55 \times 10^3 \text{ dpm m}^{-2}$

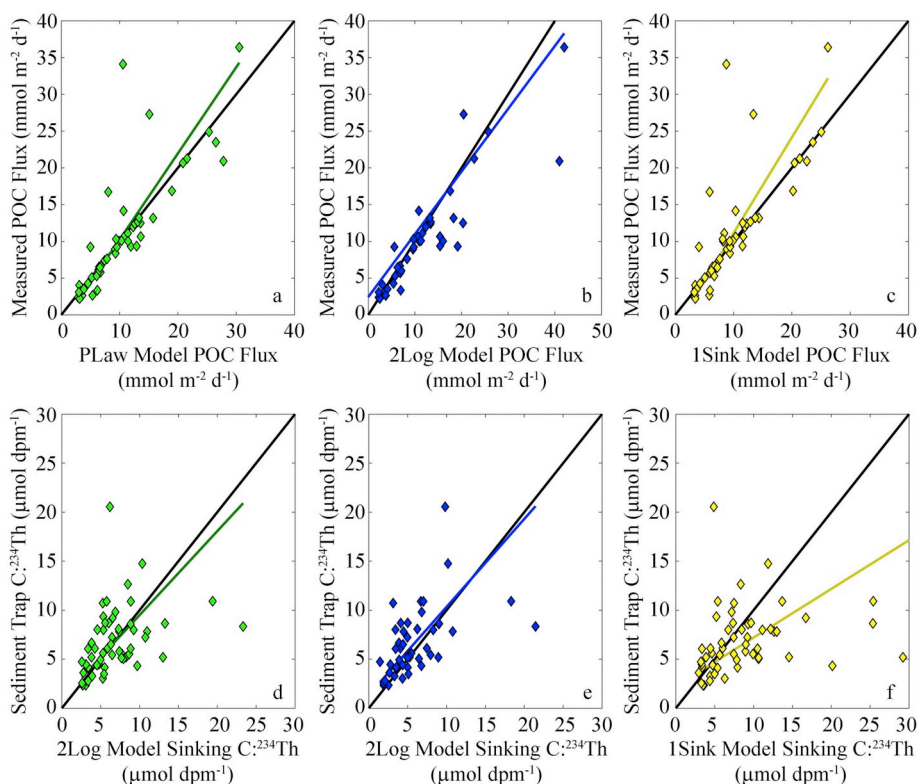


**Fig. 7.** Model-data comparison of POC flux into sediment traps (a–c) and  $C:^{234}\text{Th}$  ratios of sinking particles (d–f) for the Power Law (a, d), Double Log Normal (b, e) and Single Sinking Speed (e, f) models. Black lines are 1:1 lines. Colored lines are Type II geometric mean regressions.

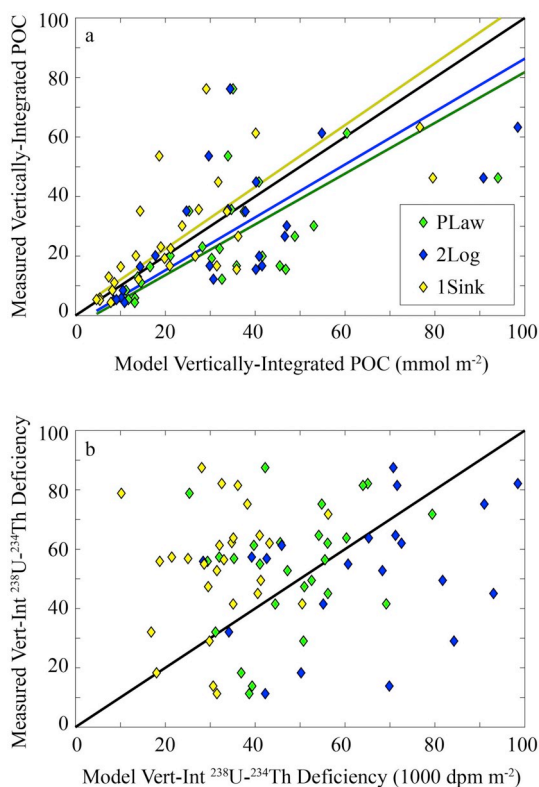


**Fig. 8.** Model-data comparison of POC vertically integrated over the upper 50 m (a) and  $^{238}\text{U}$ – $^{234}\text{Th}$  vertically integrated over the upper 100 m (b). Black lines are 1:1 lines. Colored lines are Type II geometric mean regressions.

and the mean was  $-56 \times 10^3 \text{ dpm m}^{-2}$ . For comparison, the mean and medians were  $-48 \times 10^3$  and  $-47 \times 10^3$ ,  $-65 \times 10^3$  and  $-69 \times 10^3$ , and  $-44 \times 10^3$  and  $-32 \times 10^3 \text{ dpm m}^{-2}$  for the PLaw, 2Log, and 1Sink models, respectively. However, the correlation between the model predicted and measured data was very weak. For instance, the Spearman's rank correlation was 0.39, with a  $p$ -value of 0.07. The  $p$ -value was even higher for the 1Sink and PLaw models.

We compared the efficacy with which the models predicted observed patterns in the  $C:^{234}\text{Th}$  data.  $C:^{234}\text{Th}$  ratios of sinking material decreased predictably with depth in the upper twilight zone (Eq. 17, Fig. 9a). Both the PLaw and 2Log models exhibited similar patterns of sinking particle  $C:^{234}\text{Th}$  variability with depth. Specifically,  $C:^{234}\text{Th}$  ratios decreased with depth, and the difference between samples at the base of the euphotic zone and 100 m was greater than the difference between samples at 100 m and 150 m (Fig. 9b,c). For the 1Sink model, however, the match with the data was poor and no distinct decrease in  $C:^{234}\text{Th}$  ratio with depth was seen (Fig. 9d). The agreement between *in situ* pump measured  $C:^{234}\text{Th}$  ratios and the  $C:^{234}\text{Th}$  ratios of the bulk standing stock of particles in the models were poorer. This was not unexpected because the *in situ* pump was sampling  $> 50\text{-}\mu\text{m}$  particles while the models do not differentiate particles based on size. Nevertheless, the models accurately predicted lower  $C:^{234}\text{Th}$  ratios for the standing stock of particles at a specific depth than for the flux-weighted sinking material at the same depth (Fig. 9e–h). We also tested whether the models could recover the strong relationships between the  $C:^{234}\text{Th}$  ratios of sinking material and  $^{234}\text{Th}_{\text{tot}}$ . For all models, the model predicted relationship between  $C:^{234}\text{Th}$  of sinking material and  $^{234}\text{Th}_{\text{tot}}$  was actually a better predictor of the  $C:^{234}\text{Th}$  ratio of sinking material than the relationship with the data (*i.e.* the scatter about the regression was higher for the *in situ* data than for the model results). For the PLaw and 2Log models, specifically, model  $^{234}\text{Th}_{\text{tot}}$  was a very strong predictor of model  $C:^{234}\text{Th}$ .

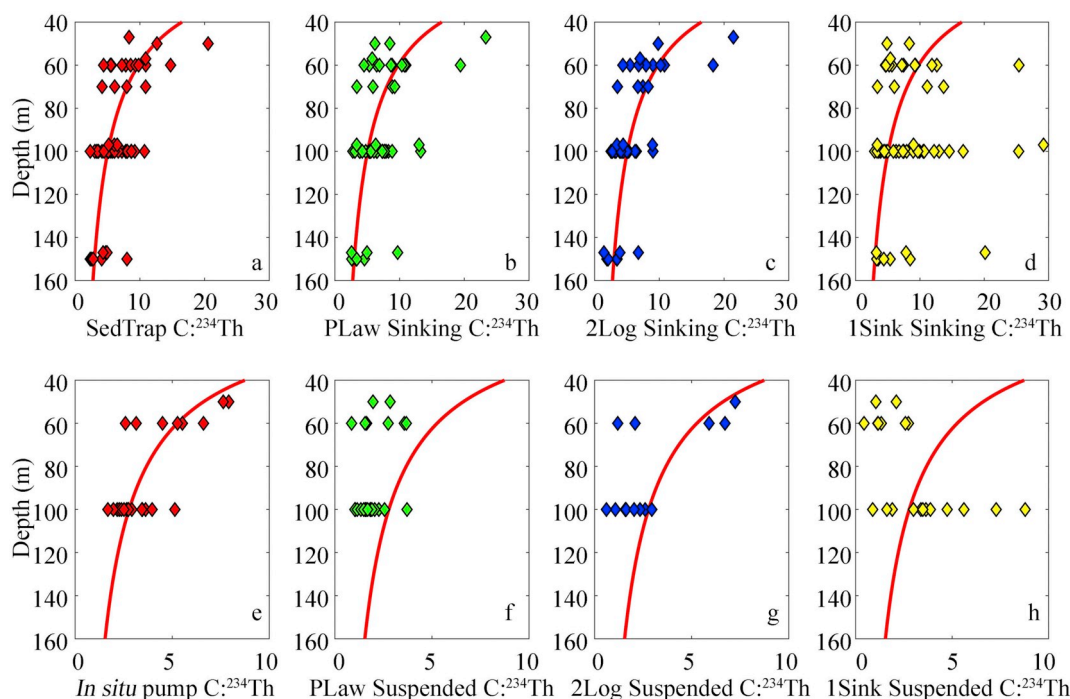


**Fig. 9.** Variation of C:<sup>234</sup>Th ratios with depth for flux-weighted sinking particles (a–d) and the standing stock of particles (e–h). a and e show *in situ* particles sampled by sediment trap and > 50- $\mu$ m *in situ* pump, respectively. b–c and f–h are model results. Model results are sampled at identical locations (i.e. identical cycle and depth) as *in situ* data. Red lines are the best-fit power law regression fits to the *in situ* data: C:<sup>234</sup>Th = 1925  $\times$  depth<sup>-1.29</sup> for sediment trap C:<sup>234</sup>Th and C:<sup>234</sup>Th = 879  $\times$  depth<sup>-1.25</sup> for the *in situ* pump C:<sup>234</sup>Th. (For interpretation of the references to colour in this figure legend, the reader is referred to the web version of this article.)

## 5. Discussion

Our primary goals in the following sections are to use the particle-thorium modeling framework to investigate the mechanisms: (1) driving the broad patterns observed in the *in situ* data and (2) creating variability about these broad patterns. In the final discussion section, we investigate model sensitivity.

### 5.1. C:<sup>234</sup>Th ratio and sinking speed

To investigate the impact of varying particle speeds with depth on C:<sup>234</sup>Th ratios we focused on the results of the 2Log model and the P1604-3 cycle. We chose the 2Log model for intensive analysis, because it performed slightly better with respect to recovering relationships between C:<sup>234</sup>Th and both depth and  $\nu$ C:<sup>234</sup>Th<sub>tot</sub>. The P1604-3 cycle was chosen because it was an average cycle with respect to primary productivity, POC, and export. Model results showed that C:<sup>234</sup>Th ratios in the mixed layer (25 m), where particle production was concentrated, were nearly constant across different particle sinking speeds (Fig. 11a). C:<sup>234</sup>Th ratios decreased with depth for all particle sinking speeds, but decreased much more rapidly for slowly-sinking particles than for rapidly-sinking particles. Thus at depths beneath the euphotic zone, C:<sup>234</sup>Th ratios increased with increasing particle sinking speed. The decrease in C:<sup>234</sup>Th ratio with depth for all particle classes was driven primarily by preferential remineralization of carbon, although adsorption of <sup>234</sup>Th from <sup>234</sup>Th enriched deeper waters also contributed. The C:<sup>234</sup>Th ratios of bulk sinking material (Fig. 11b) were determined by an interplay between the decrease in C:<sup>234</sup>Th ratios of individual particles with depth, and an increased importance of rapidly-sinking particles at deeper depths (Fig. 11c). In waters deeper than 100 m, the predominant role of rapidly-sinking particles in total flux contributed to a much lower rate of change in the C:<sup>234</sup>Th ratio with depth in these layers, which was reflected in the *in situ* data.

Few studies have directly measured the C:<sup>234</sup>Th ratio of sinking

particles as a function of sinking speed *in situ* (Buesseler et al., 2009; Jacquet et al., 2011; Stewart et al., 2007; Szlosek et al., 2009). These studies used indented rotating sphere sediment traps, which collect particles for a short duration and then release a collected batch of particles simultaneously into a chamber above a series of rotating collection cups. The results showed no clear trends in C:<sup>234</sup>Th with sinking speed, although Szlosek et al. (2009), noted that C:<sup>234</sup>Th did increase with sinking velocity in the ranges of 0.7–5.4 m d<sup>-1</sup> and for particles sinking at > 490 m d<sup>-1</sup>. They suggest that C:<sup>234</sup>Th ratio is instead determined by particle type, with fresh phytoplankton having greater C:<sup>234</sup>Th than degraded material, which is greater still than fecal pellets. Changes in the relative importance of each of these classes of particles with regard to settling velocity may explain the lack of a relationship across the entire settling velocity spectrum (Stewart et al., 2007; Szlosek et al., 2009). This explanation is plausible for the CCE, where fecal pellets are often the dominant source of sinking material (Morrow et al., 2018; Stukel et al., 2013). These pellets likely sink rapidly, but have lower C:<sup>234</sup>Th ratios than either phytoplankton or bulk POM (Rodriguez y Baena et al., 2007; Stukel et al., 2019).

Another plausible explanation for the difference between the model results and *in situ* studies is that sinking velocities are modified substantially as particles sink through the water column. Our model assumes that particles retain their settling velocities as they sink, while POM is slowly remineralized by particle-attached bacteria and <sup>234</sup>Th adsorbs, desorbs, and decays. This is clearly an oversimplification of processes that can modify sinking speeds of particles. Aggregation processes reshape sinking particles as they fall, particles are consumed and/or fragmented by deep-dwelling zooplankton and repackaged into fecal pellets, and even discrete types of particles (such as appendicularian houses) can change in settling velocity as they sink because of changes in shape and/or density (Burd and Jackson, 2009; Dilling and Ailredge, 2000; Jackson et al., 1993; Kiorboe, 2001; Robison et al., 2005; Steinberg and Landry, 2017). The indented rotating sphere sediment trap results may imply that our model needs to incorporate

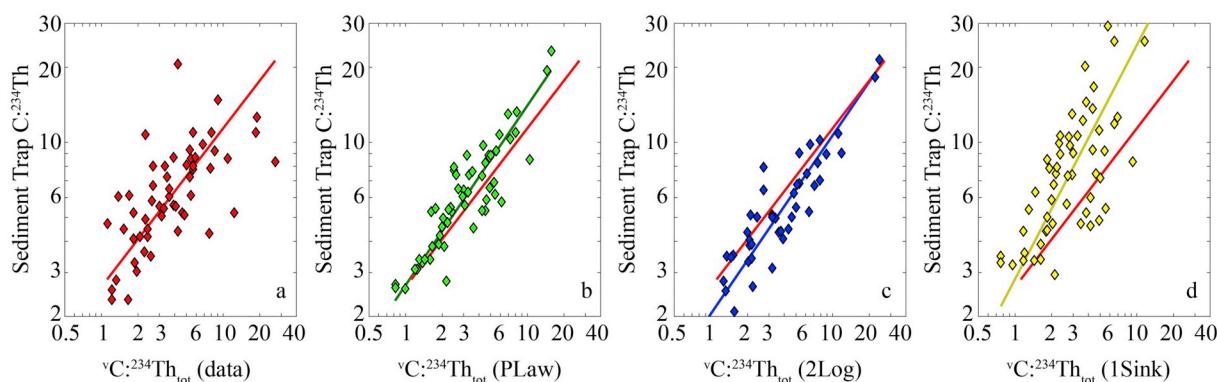


**Fig. 10.** Relation of C:<sup>234</sup>Th ratio of sinking particles to the ratio of vertically-integrated POC to vertically-integrated total water column <sup>234</sup>Th for *in situ* data (a), Power Law (b), Double Log Normal (c), and Single Sinking Speed (d) Models. Colored lines are Type II regressions for each respective dataset. Regression for *in situ* data (red) is plotted in all panels for comparison. (For interpretation of the references to colour in this figure legend, the reader is referred to the web version of this article.)

processes that re-work particles in order to more accurately simulate C:<sup>234</sup>Th ratios of sinking particles. However, we cannot rule out the possibilities that artificially high particle aggregation and disaggregation rates within the indented rotating spheres obscured patterns between C:<sup>234</sup>Th ratios and settling velocity or that patterns in the CCE (where flux is dominated by fecal pellets rather than aggregates) may be different than patterns in other regions.

### 5.2. Perturbation experiments

The model solutions presented above were all derived from simulations that were run to steady state over a course of 90 days. However, in a dynamic region such as the CCE, the ecosystem is seldom near steady state. Instead blooms constantly form in the coastal area are advected away from the coast and eventually decay offshore. This process leads to offshore advection of organic matter and a spatial decoupling of new and export production, while causing local conditions to typically exist in a state of either increasing or decreasing biomass (Olivieri and Chavez, 2000; Plattner et al., 2005). To simulate these non-steady state conditions, we ran model simulations in which we allowed the model to run to steady state for 90 days then perturbed the system. To simulate bloom formation, when phytoplankton are likely to be healthy and rapidly growing, we perturbed the model by doubling primary production. To simulate bloom decay, we perturbed the model by halving primary production, doubling the median settling velocity for small particles (*i.e.*, phytoplankton) and doubling the proportion of large particles (*i.e.* zooplankton fecal pellets) that were produced. These particular changes were made because previous CCE studies have shown that coastal bloom conditions are often dominated by rapidly growing diatoms and bloom decay is often a result of Fe stress, which leads to decreased growth rates, increased cellular Si:N and Si:C ratios, and increased sinking rates of Si-rich material packaged into rapidly sinking fecal pellets (Brzezinski et al., 2015; King and Barbeau, 2007; Stukel et al., 2017).

We ran bloom formation and bloom decay simulations for all Cycles using the Double Log Normal Model, but focus our discussion first on the “normal” cycle P1604-3. The bloom formation simulation led to a rapid increase in euphotic zone POC to slightly more than triple the initial concentrations (Fig. 12a). Total <sup>234</sup>Th activity remained relatively constant in the upper 50 m of the water column during the bloom formation (Fig. 12c). However, it increased slightly when integrated to 100 m depth. This increase was due to a substantial increase in the percentage of total water column <sup>234</sup>Th that was adsorbed onto particles and to an accumulation of slowly sinking particles immediately beneath the euphotic zone (Fig. 12e). These changes led to a steady increase in the C:<sup>234</sup>Th ratio of sinking particles over time from 8.5  $\mu\text{mol dpm}^{-1}$  to 27  $\mu\text{mol dpm}^{-1}$  at 50 m. At deeper depths, the

increase in C:<sup>234</sup>Th ratios was rapid, but plateaued quickly. At 100 m the C:<sup>234</sup>Th ratio increased from 4.5  $\mu\text{mol dpm}^{-1}$  to  $\sim 10 \mu\text{mol dpm}^{-1}$  three days after bloom initiation, but remained between 9 and 11  $\mu\text{mol dpm}^{-1}$  for the remainder of the simulation (Fig. 12g). These changes in C:<sup>234</sup>Th ratios roughly correspond to what would be expected given the simultaneous changes in  $v\text{C}:\text{Th}$  (Fig. 12i), suggesting that the C:<sup>234</sup>Th ratios was adjusting to changing water column POC and <sup>234</sup>Th.

During bloom decay, the patterns were strikingly different. POC decreased rapidly and reached a level of approximately one third of initial POC (integrated to 50 m depth) by the end of the 30-day simulation (Fig. 12b). <sup>234</sup>Th declined more gradually, as a result of the increased settling velocities and particle flux, and the percentage of <sup>234</sup>Th bound to particles declined sharply (Fig. 12d,f). Despite these changes, the C:<sup>234</sup>Th ratio remained relatively constant throughout the simulation (Fig. 12h). This was a consistent pattern across the bloom decay simulations for all Lagrangian cycles (Fig. 12j). Although  $v\text{C}:\text{Th}$  decreased substantially when the bloom crashed, high C:<sup>234</sup>Th ratios remained constant or increased as a result of rapid sinking speeds that limited POC remineralization within the upper water column. Notably, higher than expected (based on  $v\text{C}:\text{Th}$ ) C:<sup>234</sup>Th ratios during bloom decay were also predicted based on principal component analysis of the relationship of C:<sup>234</sup>Th to water column properties such as primary productivity, nutrient concentrations, and excess silica (Stukel et al., 2019). This may partly explain why the model relationship between  $v\text{C}:\text{Th}$  and C:<sup>234</sup>Th of sinking particles has less variance than the *in situ* measurements (Fig. 10). The standard model runs were sampling the system at steady state, while *in situ* conditions likely departed from steady state.

### 5.3. Particle consumption and disaggregation experiments

In our standard modeling framework, carbon is remineralized within particles, while <sup>234</sup>Th is lost from the particles only through desorption or decay. This is consistent with a conceptual framework in which particle-attached bacteria are responsible for remineralization of POC within the particles, and is fundamentally similar to how remineralization of sinking particles is accomplished in many three-dimensional biogeochemical models. However, in the environment, POC contained in sinking particles is consumed and ultimately respired by a diverse group of organisms from bacteria to fish. For instance, Steinberg et al. (2008) showed that the carbon demand of mesopelagic zooplankton was equal to that of bacteria at a station in the subarctic Pacific and Wilson et al. (2010) showed that these zooplankton were likely feeding on sinking particles. Furthermore, turbulence created by zooplankton swimming behaviors can lead to particle disaggregation in the water column (Dilling and Alldredge, 2000; Goldthwait et al.,

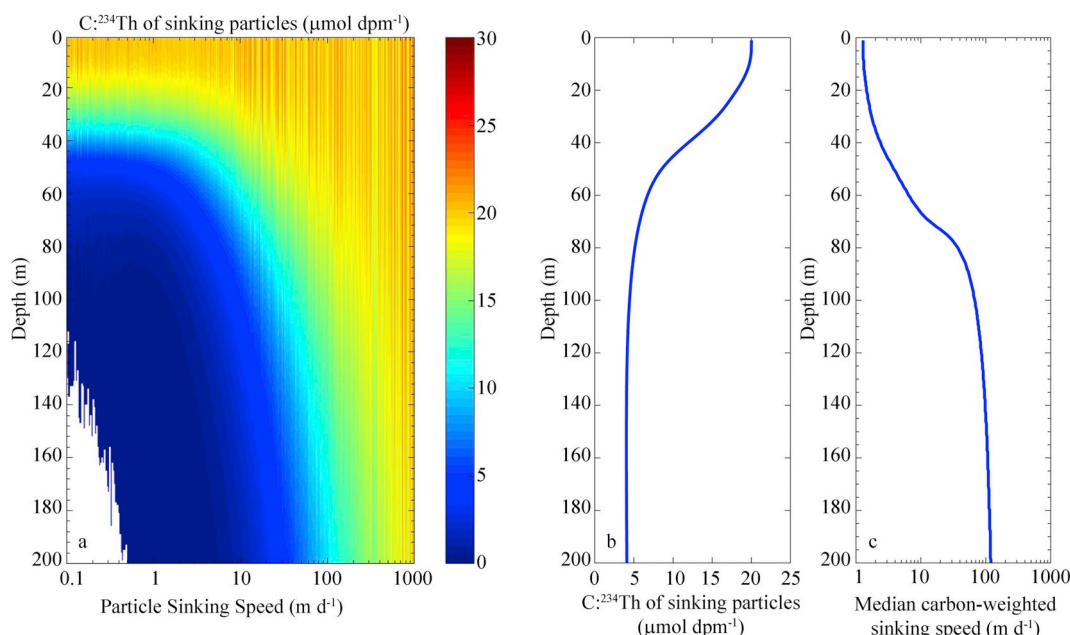


**Fig. 11.** Relationships between C:<sup>234</sup>Th ratio and sinking speed for the Double Log Normal Model and Cycle P1604-3. (a) C:<sup>234</sup>Th ratio (colour axis, μmol dpm<sup>-1</sup>) as a function of particle sinking speed (x-axis) and depth (y-axis). (b) Bulk C:<sup>234</sup>Th ratio of sinking particles versus depth. (c) Median carbon-weighted sinking speed of particles as a function of depth.

2004). Within the broader California Current Ecosystem, phaeodarians (giant protists) have been shown to (at times) intercept nearly 50% of sinking particles in the shallow twilight zone (Stukel et al., 2018a), resident populations of myctophids at mesopelagic depths have been shown to have high carbon demand (Davison et al., 2013), and giant appendicularians have been shown to feed at mesopelagic depths and produce discarded houses that contribute substantially to seafloor carbon flux (Robison et al., 2005).

These results suggest that our assumption of desorption and decay as the only loss terms for particulate <sup>234</sup>Th may oversimplify <sup>234</sup>Th cycling. To test the impact of this assumption on our results, we ran a modified version of the model in which we assumed that half of particle remineralization is mediated by organisms that entirely consume or disaggregate the particles into non-sinking colloidal material. Functionally, this was incorporated into the model by assuming a decomposition rate of <sup>234</sup>Th from the particulate to the dissolved phase that was equal to half of the calculated POC remineralization rate (i.e.,  $\gamma_{234\text{Th}} = 0.5 \times \gamma_{\text{POC}}$ ) or equal to the POC remineralization rate (i.e.,  $\gamma_{234\text{Th}} = \gamma_{\text{POC}}$ ).

Incorporating particle consumption and/or disaggregation into the model had relatively little impact (as a percentage change) on model sinking C:<sup>234</sup>Th at shallow depth horizons (e.g., 50 m), however C:<sup>234</sup>Th ratios decreased more gradually with depth than in the base model runs. For instance, with the 2Log model, the median C:<sup>234</sup>Th ratio at 50 m was 8.4 μmol dpm<sup>-1</sup> and decreased to 2.7 μmol dpm<sup>-1</sup> at 200 m. With  $\gamma_{234\text{Th}} = 0.5 \times \gamma_{\text{POC}}$ , the median ratio decreased from 9.2 μmol dpm<sup>-1</sup> at 50 m to 3.4 μmol dpm<sup>-1</sup> at 200 m. With  $\gamma_{234\text{Th}} = \gamma_{\text{POC}}$ , the median ratio decreased from 10.1 μmol dpm<sup>-1</sup> at 50 m to 4.0 μmol dpm<sup>-1</sup> at 200 m. Results were generally similar with the Power Law model (Supp. Fig. 3f,h). The relatively muted impact of this modification to the model on sinking C:<sup>234</sup>Th despite a drastic change in model structure (i.e., a switch from preferential remineralization of POC to preferential loss of <sup>234</sup>Th from particles, since <sup>234</sup>Th was lost both by consumption/disaggregation and desorption) was a result of compensatory changes in <sup>234</sup>Th activity in surface waters. Specifically, the vertically-integrated <sup>238</sup>U–<sup>234</sup>Th deficiency in the upper 100 m of the water column decreased from  $78 \times 10^3$  dpm m<sup>-2</sup> in

the base model run ( $\gamma_{234\text{Th}} = 0$ ) to  $44 \times 10^3$  dpm m<sup>-2</sup>. The additional <sup>234</sup>Th in the water column, particularly in the layer immediately below the euphotic zone thus increased <sup>234</sup>Th adsorption onto particles at deeper depths and partly compensated for increased loss of <sup>234</sup>Th from particles to the dissolved phase.

#### 5.4. Model sensitivity

We chose to test model sensitivity to not only changes in key parameters, but also to subjective *a priori* decisions about model structure. We focus these sensitivity analyses on model results pertaining to particle-thorium analyses. For a more general discussion of the sensitivity of the particle creation and sinking module, we refer readers to Stukel et al. (2018b).

We first tested model sensitivity to changes in thorium sorption and desorption parameterization by increasing and decreasing  $k_1$  and  $k_{-1}$  (see Eqs. 9 and 10) by 50% (Supp. Fig. 3a–d). Changing the sorption coefficient ( $k_1$ ) had a distinct and similar impact on C:<sup>234</sup>Th ratios with both the Double Log Normal and Power Law Models. Decreasing  $k_1$  by 50% increased C:<sup>234</sup>Th ratios of sinking particles by anywhere from ~10% to ~70%. Increasing  $k_1$  by 50% decreased C:<sup>234</sup>Th ratios by up to ~20%. With respect to the percent change in C:<sup>234</sup>Th ratios, the impact of modifying  $k_1$  had a greater impact when C:<sup>234</sup>Th ratios were low. During periods with high POC concentrations, the C:<sup>234</sup>Th ratios of sinking particles were less sensitive to modifications in  $k_1$ . It is important to note that the actual *in situ* value of  $k_1$  is highly uncertain. The value that we used was a median value derived from CCE field data (Stukel et al., 2019), and was not dissimilar from the value used by Resplandy et al. (2012). Previously published estimates from different regions, however, have varied by two orders of magnitude (see Murnane et al., 1994 and references therein).  $k_1$  is likely to vary substantially in the ocean, because <sup>234</sup>Th adsorption should actually be expected to co-vary with the concentration of binding sites for thorium, rather than with POC. Variables potentially affecting  $k_1$  include the concentration of acid polysaccharides and humic acids, the ratio of lithogenic material to organic matter, the ratio of colloids to particles, the particle size spectrum, the fractal dimensions of aggregates, and pH

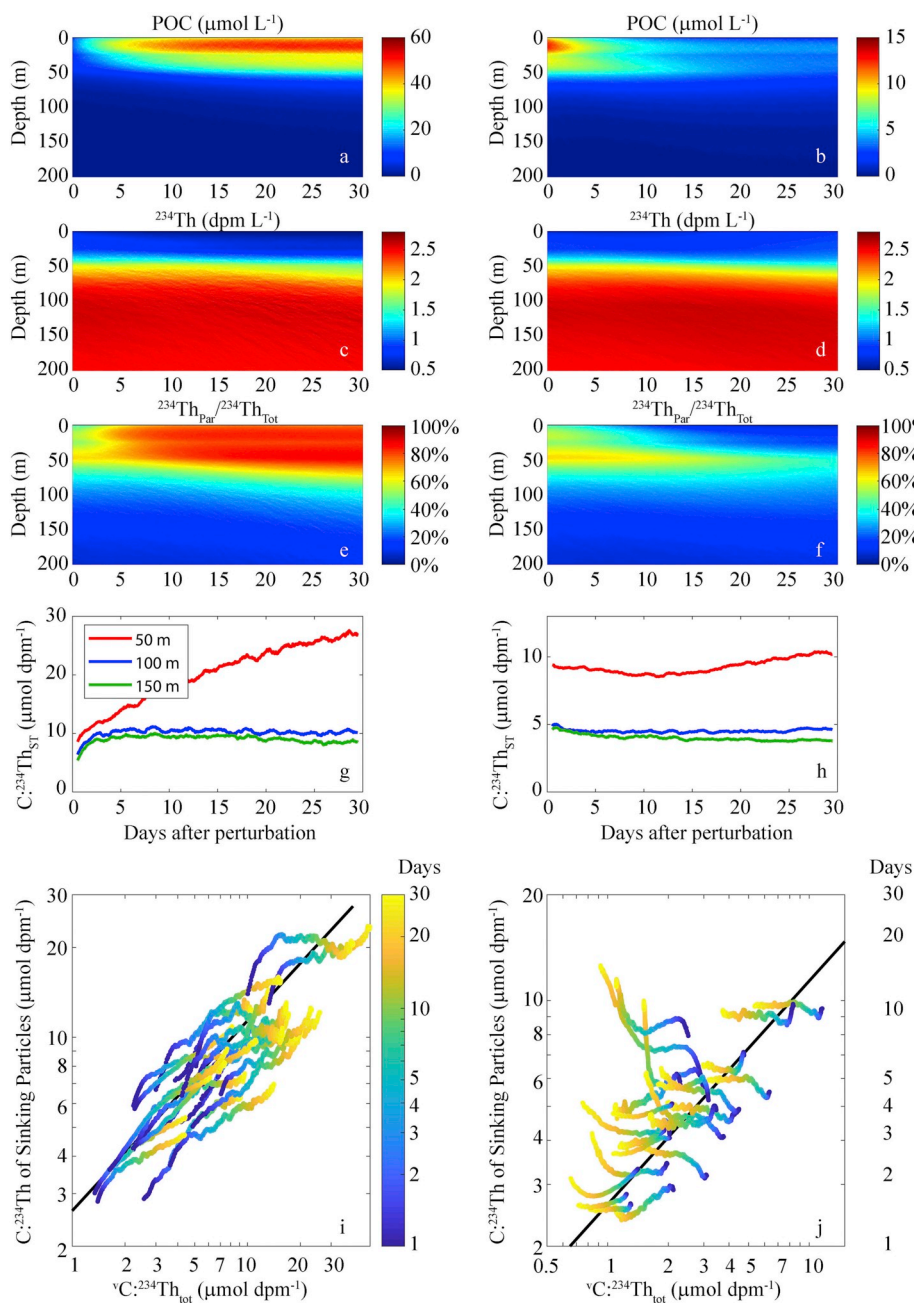


**Fig. 12.** Results of non-steady state perturbation experiments for the 2Log Model. (a and b) POC concentrations versus time after perturbation and depth. (c and d)  $^{234}\text{Th}_{\text{tot}}$  activity versus time after perturbation and depth. (e and f) Percentage of  $^{234}\text{Th}$  adsorbed onto particles. (g and h)  $C:^{234}\text{Th}$  ratios of sinking particles versus time after perturbation. a–h are results for Cycle P1604-3. a, c, e, and g simulate bloom formation. b, d, f, and h simulate bloom decay. i and j)  $C:^{234}\text{Th}$  ratio of sinking particles (at 100 m depth) versus ratio of vertically-integrated POC to vertically-integrated total water column  $^{234}\text{Th}$  ( $^{\circ}C:^{234}\text{Th}_{\text{tot}}$ ). Colour axis is days after perturbation. Black lines are a Type II regression of  $C:^{234}\text{Th}_{\text{ST}}$  against  $^{\circ}C:^{234}\text{Th}_{\text{tot}}$  for *in situ* data (see Fig. 10a). i simulates bloom formation (all cycles) and j simulates bloom decay (all cycles).

(Burd et al., 2007; Guo et al., 2002; Honeyman et al., 1988; Murphy et al., 1999; Passow et al., 2006; Quigley et al., 2002; Santschi et al., 2006).

By contrast, the model was much less sensitive to changes in the desorption coefficient ( $k_{-1}$ ). For both models, increasing or decreasing  $k_{-1}$  by 50% led to less than a 10% change in  $C:^{234}\text{Th}$  ratios. This is not surprising, because even if the desorption coefficient was increased by 50% (from  $3 \text{ yr}^{-1}$  to  $4.5 \text{ yr}^{-1}$ ), the dominant loss term for  $^{234}\text{Th}$  from sinking particles was radioactive decay ( $\lambda_{234} = 10.5 \text{ yr}^{-1}$ ).

The model results were only moderately sensitive to changes in model structure to allow for the consumption and/or disaggregation of particles by mesozooplankton (Supp. Fig. 3e–h). Crucially, this modification shifted the design of the model from one with very strong preferential remineralization of carbon from particles (base model,  $\gamma_{234\text{Th}} = 0$ ) to a version with mild preferential remineralization of carbon ( $\gamma_{234\text{Th}} = 0.5 \times \gamma_{\text{POC}}$ ) or with preferential remineralization of  $^{234}\text{Th}$  ( $\gamma_{234\text{Th}} = \gamma_{\text{POC}}$ ). Despite these drastic changes,  $C:^{234}\text{Th}$  ratios

typically changed by no more than a factor of 2 (for the version of the models with  $\gamma_{234\text{Th}} = \gamma_{\text{POC}}$ ). As with the changes to  $k_1$ , these impacts were most apparent when POC concentrations were comparatively low and hence  $C:^{234}\text{Th}$  ratios were fairly low.

Modifying the shape of the particle settling velocity spectrum (when using realistic spectra, *i.e.* the Power Law or Double Log Normal Models) had a comparable impact on  $C:^{234}\text{Th}$  ratios, leading to up to a doubling or halving of  $C:^{234}\text{Th}$ . Notably, there was not a consistent offset between the  $C:^{234}\text{Th}$  ratios predicted by the Power Law and Double Log Normal Models. Instead, the Double Log Normal Model tended to predict higher  $C:^{234}\text{Th}$  ratios for sinking particles at shallow depths, while the Power Law Model predicted higher  $C:^{234}\text{Th}$  ratios at deeper depths (Fig. 9b,c and Supp. Fig. 3i).

In contrast, the use of an unrealistic settling velocity spectrum (Single Sinking Speed Model set sinking speeds to either 0 or  $100 \text{ m d}^{-1}$ ), led to very different patterns in  $C:^{234}\text{Th}$  ratios (Supp. Fig. 3j). Specifically, it predicted almost no change in  $C:^{234}\text{Th}$  ratios with depth

(Fig. 9d). This unrealistic pattern was driven by the fact that particles sinking at  $100 \text{ m d}^{-1}$  exited the model domain in less than 2 days, and hence did not have sufficient time for substantial modification of their  $\text{C}^{234}\text{Th}$  ratios as they sank. Both the Power Law and Double Log Normal Models featured different contributions of particles with different sinking speeds at different depths, with concomitantly different  $\text{C}^{234}\text{Th}$  ratios. These results highlight the importance of including a broader range of particle sinking speeds in biogeochemical models.

## 6. Conclusions

A simple thorium sorption and desorption model, coupled to models of particle formation and sinking (parameterized with realistic distributions of particle settling velocities) predicted realistic  $\text{C}^{234}\text{Th}$  ratios for sinking particles in the CCE. The performance of this simple modeling framework lends encouragement to studies that incorporate such  $^{234}\text{Th}$  frameworks into biogeochemical models (e.g., Resplandy et al., 2012). It also suggests that broad patterns in  $\text{C}^{234}\text{Th}$  ratios (e.g. the correlation between the  $\text{C}^{234}\text{Th}$  ratios of sinking particles and the ratio of vertically-integrated POC to vertically integrated  $^{234}\text{Th}_{\text{tot}}$ ) may be driven by preferential remineralization of carbon and varying sinking speeds of particles. Notably, the 1Sink Model (which assigned a sinking speed of  $100 \text{ m d}^{-1}$  for all sinking particles) did not accurately estimate the decrease in  $\text{C}^{234}\text{Th}$  ratios with depth. Nevertheless, substantial unexplained variability remains and may be driven in part by non-steady state conditions frequently encountered in this dynamic coastal region, or the role of mesozooplankton in disaggregating or consuming sinking particles and the  $^{234}\text{Th}$  contained within. Furthermore, a model without preferential remineralization of carbon was similarly able to estimate decreasing  $\text{C}^{234}\text{Th}$  ratios with depth (although this version of the model showed slower decreases with depth) as a result of continual  $^{234}\text{Th}$  sorption to particles as they sink. Additional fieldwork including measurements of  $\text{C}^{234}\text{Th}$  ratios as a function of sinking speed and/or particle size and investigation into the relative importance of particle-attached bacteria or particle-consuming zooplankton are necessary to differentiate between different mechanisms that may drive changes in  $\text{C}^{234}\text{Th}$  ratios with depth.

The results of our sensitivity analyses also make it clear that determination of the processes driving variability in the adsorption coefficient ( $k_1$ ) should be a priority for future research.  $k_1$  is likely affected by a suite of parameters including particle size, acid polysaccharide and humic acid concentration, and pH.  $k_1$  needs to be determined across a range of ecosystems that vary with respect to these parameters and others. Importantly, attempts to determine  $k_1$  from *in situ* data should, at a minimum, measure profiles of dissolved and particulate thorium (preferably in multiple size fractions) and POC, while also making an independent measure of particle flux (e.g., using sediment traps) to ensure that the  $^{238}\text{U}$ – $^{234}\text{Th}$  steady-state assumption can be tested. These measurements should be assimilated into second-order rate kinetic models to quantify  $k_1$  (and potentially other parameters of more complex models that include such processes as intermediate incorporation of thorium into colloids and aggregation/disaggregation between size classes). Variability in these parameters can then be objectively compared to simultaneous measurements of the processes believed to drive their variability. Such progress will clearly require carefully planned studies involving biologists, organic and trace metal biogeochemists, and modelers.

## Acknowledgments

We thank the captains and crew of the R/V Melville, Thompson, and Sikuliaq for making this work possible. We also thank Peter Morton and Vincent Salters for assistance with ICP-MS measurements and Claudia Benitez-Nelson for extensive assistance with  $^{234}\text{Th}$  analyses on the P0704, P0810, and P1106 Cruises. We are deeply indebted to our many colleagues within the CCE LTER who contributed to sample collection

and analysis. Data used in this manuscript are freely available on the CCE LTER Datazoo website: <https://oceaninformatics.ucsd.edu/datazoo/catalogs/ccelter/datasets>. This work was supported by NSF Bio Oce grants to the CCE LTER Program: OCE-0417616, OCE-1026607, OCE-1637632, and OCE-1614359. A portion of this work was performed at the National High Magnetic Field Laboratory, which is supported by National Science Foundation Cooperative Agreement No. DMR-1644779 and the State of Florida.

## Appendix A. Supplementary data

Supplementary data to this article can be found online at <https://doi.org/10.1016/j.marchem.2019.03.005>.

## References

- Armstrong, R.A., Peterson, M.L., Lee, C., Wakeham, S.G., 2009. Settling velocity spectra and the ballast ratio hypothesis. *Deep-Sea Res. II* 56 (18), 1470–1478.
- Benitez-Nelson, C.R., et al., 2001. Testing a new small-volume technique for determining Th-234 in seawater. *J. Radioanal. Nucl. Chem.* 248 (3), 795–799.
- Bhat, S.G., Krishnaswamy, S., Lal, D., Rama and Moore, W.S., 1968.  $^{234}\text{Th}/^{238}\text{U}$  ratios in the ocean. *Earth Planet. Sci. Lett.* 5, 483–491.
- Black, E.E., Buesseler, K.O., Pike, S.M., Lam, P.J., 2018.  $^{234}\text{Th}$  as a tracer of particulate export and remineralization in the southeastern tropical Pacific. *Mar. Chem.* 201, 35–50.
- Brzezinski, M.A., et al., 2015. Enhanced silica ballasting from iron stress sustains carbon export in a frontal zone within the California Current. *J. Geophys. Res. Oceans* 120 (7), 4654–4669.
- Buesseler, K.O., Bacon, M.P., Cochran, J.K., Livingston, H.D., 1992. Carbon and nitrogen export during the JGOFS North Atlantic Bloom Experiment estimated from  $^{234}\text{Th}$ – $^{238}\text{U}$  disequilibrium. *Deep-Sea Res.* 39 (7–8A), 1115–1137.
- Buesseler, K.O., et al., 2006. An assessment of particulate organic carbon to thorium-234 ratios in the ocean and their impact on the application of  $^{234}\text{Th}$  as a POC flux proxy. *Mar. Chem.* 100 (3–4), 213–233.
- Buesseler, K.O., et al., 2007. An assessment of the use of sediment traps for estimating upper ocean particle fluxes. *J. Mar. Res.* 65 (3), 345–416.
- Buesseler, K.O., et al., 2009. Thorium-234 as a tracer of spatial, temporal and vertical variability in particle flux in the North Pacific. *Deep-Sea Res. I Oceanogr. Res. Pap.* 56 (7), 1143–1167.
- Burd, A.B., Jackson, G.A., 2009. Particle aggregation. *Annu. Rev. Mar. Sci.* 1, 65–90.
- Burd, A.B., Jackson, G.A., Moran, S.B., 2007. The role of the particle size spectrum in estimating POC fluxes from Th-234/U-238 disequilibrium. *Deep-Sea Res. I* 54 (6), 897–918.
- Coale, K.H., Bruland, K.W., 1985. Th-234 – U-238 disequilibrium within the California Current. *Limnol. Oceanogr.* 30 (1), 22–33.
- Conover, R.J., 1966. Assimilation of organic matter by zooplankton. *Limnol. Oceanogr.* 11 (3), 338–345.
- Davison, P.C., Checkley, D.M., Koslow, J.A., Barlow, J., 2013. Carbon export mediated by mesopelagic fishes in the Northeast Pacific Ocean. *Prog. Oceanogr.* 116, 14–30.
- Dilling, L., Alldredge, A.L., 2000. Fragmentation of marine snow by swimming macrozooplankton: a new process impacting carbon cycling in the sea. *Deep-Sea Res. I* 47 (7), 1227–1245.
- Ducklow, H.W., et al., 2018. Spring-summer net community production, new production, particle export and related water column biogeochemical processes in the marginal sea ice zone of the Western Antarctic Peninsula 2012–2014. *Philos. Trans. R. Soc. Lond. A* 376.
- Dunne, J.P., Murray, J.W., Young, J., Balistrieri, L.S., Bishop, J., 1997. Th-234 and particle cycling in the central equatorial Pacific. *Deep-Sea Res. Part II-Top. Stud. Oceanogr.* 44 (9–10), 2049–2083.
- Durkin, C.A., Estapa, M.L., Buesseler, K.O., 2015. Observations of carbon export by small sinking particles in the upper mesopelagic. *Mar. Chem.* 175, 72–81.
- Estapa, M.L., et al., 2015. Decoupling of net community and export production on sub-mesoscales. *Glob. Biogeochem. Cycles* 29 (8), 1266–1282.
- Goldthwait, S., Yen, J., Brown, J., Alldredge, A., 2004. Quantification of marine snow fragmentation by swimming euphausiids. *Limnol. Oceanogr.* 49 (4), 940–952.
- Guo, L., Hung, C.-C., Santschi, P.H., Walsh, I.D., 2002.  $^{234}\text{Th}$  scavenging and its relationship to acid polysaccharide abundance in the Gulf of Mexico. *Mar. Chem.* 78 (2–3), 103–119.
- Hayes, C.T., et al., 2015. Thorium isotopes tracing the iron cycle at the Hawaii Ocean Time-series Station ALOHA. *Geochim. Cosmochim. Acta* 169, 1–16.
- Honeyman, B.D., Balistrieri, L.S., Murray, J.W., 1988. Oceanic trace metal scavenging: the importance of particle concentration. *Deep Sea Res. Part A. Oceanogr. Res. Pap.* 35 (2), 227–246.
- Hung, C.-C., Guo, L., Roberts, K.A., Santschi, P.H., 2004. Upper ocean carbon flux determined by the  $^{234}\text{Th}$  approach and sediment traps using size-fractionated POC and  $^{234}\text{Th}$  data from the Gulf of Mexico. *Geochim. J.* 38 (6), 601–611.
- Hung, C.C., Gong, G.C., Santschi, P.H., 2012. Th-234 in different size classes of sediment trap collected particles from the Northwestern Pacific Ocean. *Geochim. Cosmochim. Acta* 91, 60–74.
- Jackson, G.A., Burd, A.B., 2015. Simulating aggregate dynamics in ocean biogeochemical models. *Prog. Oceanogr.* 133, 55–65.

- Jackson, G.A., Najjar, R.G., Toggweiler, J.R., 1993. Flux feeding as a mechanism for zooplankton grazing and its implications for vertical particulate flux. *Limnol. Oceanogr.* 38 (6), 1328–1331.
- Jacquet, S., Lam, P., Trull, T., Dehairs, F., 2011. Carbon export production in the sub-antarctic zone and polar front zone south of Tasmania. *Deep-Sea Res. II Top. Stud. Oceanogr.* 58 (21–22), 2277–2292.
- King, A.L., Barbeau, K., 2007. Evidence for phytoplankton iron limitation in the southern California Current System. *Mar. Ecol. Prog. Ser.* 342, 91–103.
- Kiorboe, T., 2001. Formation and fate of marine snow: small-scale processes with large-scale implications. *Sci. Mar.* 65, 57–71.
- Knauer, G.A., Martin, J.H., Bruland, K.W., 1979. Fluxes of particulate carbon, nitrogen, and phosphorus in the upper water column of the Northeast Pacific. *Deep-Sea Res.* 26 (1), 97–108.
- Krause, J.W., et al., 2015. Variability in diatom contributions to biomass, organic matter production and export across a frontal gradient in the California Current Ecosystem. *J. Geophys. Res. Oceans* 120 (2), 1032–1047.
- Landry, M.R., Ohman, M.D., Goericke, R., Stukel, M.R., Tsyrlkevich, K., 2009. Lagrangian studies of phytoplankton growth and grazing relationships in a coastal upwelling ecosystem off Southern California. *Prog. Oceanogr.* 83, 208–216.
- Landry, M.R., et al., 2012. Pelagic community responses to a deep-water front in the California Current Ecosystem: overview of the A-front study. *J. Plankton Res.* 34 (9), 739–748.
- Lerner, P., et al., 2016. Testing models of thorium and particle cycling in the ocean using data from station GT11-22 of the US GEOTRACES North Atlantic section. *Deep-Sea Res. I Oceanogr. Res. Pap.* 113, 57–79.
- Luo, S.D., Ku, T.L., Kusakabe, M., Bishop, J.K.B., Yang, Y.L., 1995. Tracing particle cycling in the Upper Ocean with Th-230 and Th-228 – an investigation in the equatorial Pacific along 140-degrees-W. *Deep-Sea Res. Part II-Top. Stud. Oceanogr.* 42 (2–3), 805–829.
- McDonnell, A.M.P., Buesseler, K.O., 2010. Variability in the average sinking velocity of marine particles. *Limnol. Oceanogr.* 55 (5), 2085–2096.
- Morrow, R.M., et al., 2018. Primary productivity, mesozooplankton grazing, and the biological pump in the California Current Ecosystem: variability and response to El Niño. *Deep-Sea Res. I* 140, 52–62.
- Murnane, R., Cochran, J., Sarmiento, J., 1994. Estimates of particle-and thorium-cycling rates in the Northwest Atlantic Ocean. *J. Geophys. Res.: Oceans* 99 (C2), 3373–3392.
- Murphy, R.J., Lenhart, J.J., Honeyman, B.D., 1999. The sorption of thorium (IV) and uranium (VI) to hematite in the presence of natural organic matter. *Colloids Surf. A Physicochem. Eng. Asp.* 157 (1–3), 47–62.
- Nickels, C.F., Ohman, M.D., 2018. CCEIII: persistent functional relationships between copepod egg production rates and food concentration through anomalously warm conditions in the California Current Ecosystem. *Deep Sea Res. I* 140, 26–35.
- Olivieri, R.A., Chavez, F.P., 2000. A model of plankton dynamics for the coastal upwelling system of Monterey Bay, California. *Deep-Sea Res. II* 47 (5–6), 1077–1106.
- Owens, S.A., Buesseler, K.O., Sims, K.W.W., 2011. Re-evaluating the  $^{238}\text{U}$ -salinity relationship in seawater: implications for the  $^{238}\text{U}$ - $^{234}\text{Th}$  disequilibrium method. *Mar. Chem.* 127 (1–4), 31–39.
- Owens, S.A., Pike, S., Buesseler, K.O., 2015. Thorium-234 as a tracer of particle dynamics and upper ocean export in the Atlantic Ocean. *Deep-Sea Res. II* 116, 42–59.
- Passow, U., Dunne, J., Murray, J.W., Balistrieri, L., Alldredge, A.L., 2006. Organic carbon to Th-234 ratios of marine organic matter. *Mar. Chem.* 100 (3–4), 323–336.
- Pike, S.M., Buesseler, K.O., Andrews, J., Savoye, N., 2005. Quantification of  $^{234}\text{Th}$  recovery in small volume sea water samples by inductively coupled plasma-mass spectrometry. *J. Radioanal. Nucl. Chem.* 263 (2), 355–360.
- Plattner, G.K., Gruber, N., Frenzel, H., McWilliams, J.C., 2005. Decoupling marine export production from new production. *Geophys. Res. Lett.* <https://doi.org/10.1029/2005GL022660>.
- Puigcorb , V., et al., 2017. Latitudinal distributions of particulate carbon export across the North Western Atlantic Ocean. *Deep-Sea Res. I Oceanogr. Res. Pap.* 129 (Supplement C), 116–130.
- Quigley, M.S., Santschi, P.H., Hung, C.-C., Guo, L., Honeyman, B.D., 2002. Importance of acid polysaccharides for  $^{234}\text{Th}$  complexation to marine organic matter. *Limnol. Oceanogr.* 47 (2), 367–377.
- Reiller, P., Moulin, V., Casanova, F., Dautel, C., 2003. On the study of Th (IV)-humic acid interactions by competition sorption studies with silica and determination of global interaction constants. *Radiochim. Acta* 91 (9), 513–524.
- Reiller, P.E., Evans, N.D., Szabo, G., 2008. Complexation parameters for the actinides (IV)-humic acid system: a search for consistency and application to laboratory and field observations. *Radiochim. Acta* 96 (6), 345–358.
- Resplandy, L., et al., 2012. How does dynamical spatial variability impact  $^{234}\text{Th}$ -derived estimates of organic export? *Deep-Sea Res. I* 68, 24–45.
- Robison, B.H., Reisenbichler, K.R., Sherlock, R.E., 2005. Giant larvacean houses: rapid carbon transport to the deep sea floor. *Science* 308 (5728), 1609–1611.
- Rodr guez y Baena, A.M., Fowler, S.W., Miquel, J.C., 2007. Particulate organic carbon: natural radionuclide ratios in zooplankton and their freshly produced fecal pellets from the NW Mediterranean (MedFlux 2005). *Limnol. Oceanogr.* 52 (3), 966–974.
- Santschi, P.H., et al., 2006. Thorium speciation in seawater. *Mar. Chem.* 100 (3–4), 250–268.
- Savoye, N., et al., 2006.  $^{234}\text{Th}$  sorption and export models in the water column: a review. *Mar. Chem.* 100 (3–4), 234–249.
- Shaw, T.J., Smoak, J.M., Lauerma, L., 1998. Scavenging of ex( $^{234}\text{Th}$ ), ex( $^{230}\text{Th}$ ), and ex( $^{210}\text{Pb}$ ) by particulate matter in the water column of the California Continental Margin. *Deep-Sea Res. Part II-Top. Stud. Oceanogr.* 45 (4–5), 763–779.
- Smayda, T.J., Bienfang, P.K., 1983. Suspension properties of various phyletic groups of phytoplankton and tintinnids in an oligotrophic subtropical system. *Mar. Ecol. 4* (4), 289–300.
- Steinberg, D.K., Landry, M.R., 2017. Zooplankton and the ocean carbon cycle. *Annu. Rev. Mar. Sci.* 9, 413–444.
- Steinberg, D.K., et al., 2008. Bacterial vs. zooplankton control of sinking particle flux in the ocean's twilight zone. *Limnol. Oceanogr.* 53 (4), 1327–1338.
- Stewart, G., et al., 2007. Comparing POC export from  $^{234}\text{Th}/^{238}\text{U}$  and  $^{210}\text{Po}/^{210}\text{Pb}$  disequilibria with estimates from sediment traps in the Northwest Mediterranean. *Deep-Sea Res. I Oceanogr. Res. Pap.* 54 (9), 1549–1570.
- Stukel, M.R., Landry, M.R., Benitez-Nelson, C.R., Goericke, R., 2011. Trophic cycling and carbon export relationships in the California Current Ecosystem. *Limnol. Oceanogr.* 56 (5), 1866–1878.
- Stukel, M.R., Ohman, M.D., Benitez-Nelson, C.R., Landry, M.R., 2013. Contributions of mesozooplankton to vertical carbon export in a coastal upwelling system. *Mar. Ecol. Prog. Ser.* 491, 47–65.
- Stukel, M.R., et al., 2017. Mesoscale Ocean fronts enhance carbon export due to gravitational sinking and subduction. *Proc. Natl. Acad. Sci.* 114 (6), 1252–1257.
- Stukel, M.R., Biard, T., Krause, J.W., Ohman, M.D., 2018a. Large Phaeodaria in the twilight zone: their role in the carbon cycle. *Limnol. Oceanogr.* 63, 2579–2594.
- Stukel, M.R., Song, H., Goericke, R., Miller, A.J., 2018b. The role of subduction and gravitational sinking in particle export, carbon sequestration, and the remineralization length scale in the California Current Ecosystem. *Limnol. Oceanogr.* 63 (1), 363–383.
- Stukel, M.R., et al., 2019. The Carbon: $^{234}\text{Thorium}$  ratios of sinking particles in the California Current Ecosystem 1: relationships with plankton ecosystem dynamics. *Mar. Chem.* <https://doi.org/10.1016/j.marchem.2019.01.003>.
- Szlosek, J., et al., 2009. Particulate organic carbon-Th-234 relationships in particles separated by settling velocity in the Northwest Mediterranean Sea. *Deep-Sea Res. Part II-Top. Stud. Oceanogr.* 56 (18), 1519–1532.
- Turner, J.T., 2002. Zooplankton fecal pellets, marine snow and sinking phytoplankton blooms. *Aquat. Microb. Ecol.* 27 (1), 57–102.
- Turner, J.T., 2015. Zooplankton fecal pellets, marine snow, phytodetritus and the ocean's biological pump. *Prog. Oceanogr.* 130 (0), 205–248.
- van der Loeff, M.R., et al., 2011. Th-234 in surface waters: distribution of particle export flux across the Antarctic circumpolar current and in the Weddell Sea during the GEOTRACES expedition ZERO and DRAKE. *Deep-Sea Res. Part II-Top. Stud. Oceanography* 58 (25–26), 2749–2766.
- Waples, J.T., et al., 2006. An introduction to the application and future use of  $^{234}\text{Th}$  in aquatic systems. *Mar. Chem.* 100 (3–4), 166–189.
- Wilson, S.E., Steinberg, D.K., Chu, F.L.E., Bishop, J.K.B., 2010. Feeding ecology of mesopelagic zooplankton of the subtropical and subarctic North Pacific Ocean determined with fatty acid biomarkers. *Deep-Sea Res. I* 57 (10), 1278–1294.